IEEE Access
Multidisciplinary ⋮ Rapid Review ⋮ Open Access Journal

Received January 13, 2022, accepted February 8, 2022, date of publication February 22, 2022, date of current version March 11, 2022.

Digital Object Identifier 10.1109/ACCESS.2022.3153492

Feasibility Study of a W-Band Multibeam Heterodyne Receiver for the Gregorian Focus of the Sardinia Radio Telescope

A. NAVARRINI[1], L. OLMI[2], R. NESTI[2], P. ORTU[1], P. MARONGIU[1], A. ORLATI[3], A. SCALAMBRA[3], A. ORFEI[3], J. RODA[3], A. CATTANI[3], S. LEURINI[1], F. GOVONI[1], M. MURGIA[1], E. CARRETTI[3], D. FIERRO[4], AND A. PELLIZZONI[1]

[1]Istituto Nazionale di Astrofisica (INAF)-Osservatorio Astronomico di Cagliari, 09047 Selargius, Cagliari, Italy
[2]Istituto Nazionale di Astrofisica (INAF)-Osservatorio Astrofisico di Arcetri, 50125 Firenze, Italy
[3]Istituto Nazionale di Astrofisica (INAF)-Istituto di Radiastronomia, 40129 Bologna, Italy
[4]Direzione Scientifica, Istituto Nazionale di Astrofisica (INAF)-Ufficio Ingegneristico Centrale, 00136 Roma, Italy

Corresponding author: A. Navarrini (alessandro.navarrini@inaf.it)

This work was supported by the National Operative Program (Programma Operativo Nazionale-PON) of the Italian Ministry of University and Research, Notice D.D. 424 of 28/02/2018, for the granting of funding aimed at strengthening research infrastructures, in implementation of the Action II.1 [Enhancement of the Sardinia Radio Telescope (SRT) for the study of the Universe at High Radio Frequencies], under Project PIR01_00010.

ABSTRACT We report on the feasibility study of a W-band multibeam heterodyne receiver for the Sardinia Radio Telescope (SRT), a general purpose fully steerable 64-m diameter antenna located on the Sardinia island, Italy, managed by INAF (''Istituto Nazionale di Astrofisica,'' Italy). The W-band front-end is designed for the telescope Gregorian focal plane and will detect both continuum and molecular spectral lines from astronomical sources and radio emission from the Sun in the 3 mm atmospheric window. The goal specification of the receiver is a 4×4 focal plane array operating in dual-linear polarization with a front-end consisting of feed-horns placed in cascade with waveguide Orthomode Transducers (OMTs) and LNAs (Low Noise Amplifiers) cryogenically cooled at $\approx$20 K. The instantaneous FoV (Field of View) of the telescope is limited by the shaping of the 64-m primary and 7.9-m secondary mirrors. The cryogenic modules are designed to fit in the usable area of the focal plane and provide high-quality beam patterns with high antenna efficiency across the $70 - 116$ GHz Radio Frequency (RF) band. The FoV covered by the 4×4 array is 2.15×2.15 arcmin^2, unfilled, with separation between contiguous elements of 43 arcsec. Dual-sideband separation (2SB) down-conversion mixers are designed to be placed at the cryostat output and arranged in four four-pixel down-conversion modules with $4 - 12$ GHz Intermediate Frequency (IF) bands (both Upper Side Band and Lower Side Band selectable for any pixel and polarization). The receiver utilizes a mechanical derotator to track the parallactic angle.

INDEX TERMS Array, cryogenics, derotator, down-converter, feed-horn, front end, low noise amplifier, mixer, multibeam, orthomode transducer, sideband separation, radio astronomy, receiver.

I. INTRODUCTION TO THE SRT

The Sardinia Radio Telescope (SRT, www.srt.inaf.it) is a general-purpose fully steerable 64-m diameter radio telescope designed to operate with high efficiency across the $0.3 - 116$ GHz frequency range [1]–[4]. The radio observatory is the result of the scientific and technical collaboration among three separate organizations of INAF (www.inaf.it): the ''Istituto di Radioastronomia'' (IRA), the ''Osservatorio Astronomico di Cagliari'' (OAC), and the ''Osservatorio Astrofisico di Arcetri'' (OAA). The main funding agencies are the Italian Ministry of University and Research (MUR), the Sardinia Regional Government (RAS), the Italian Space Agency (ASI), and INAF itself. The SRT is designed to be used for astronomy, geodesy and space science, both as a single dish and as part of European and International VLBI (Very

The associate editor coordinating the review of this manuscript and approving it for publication was Derek Abbott.

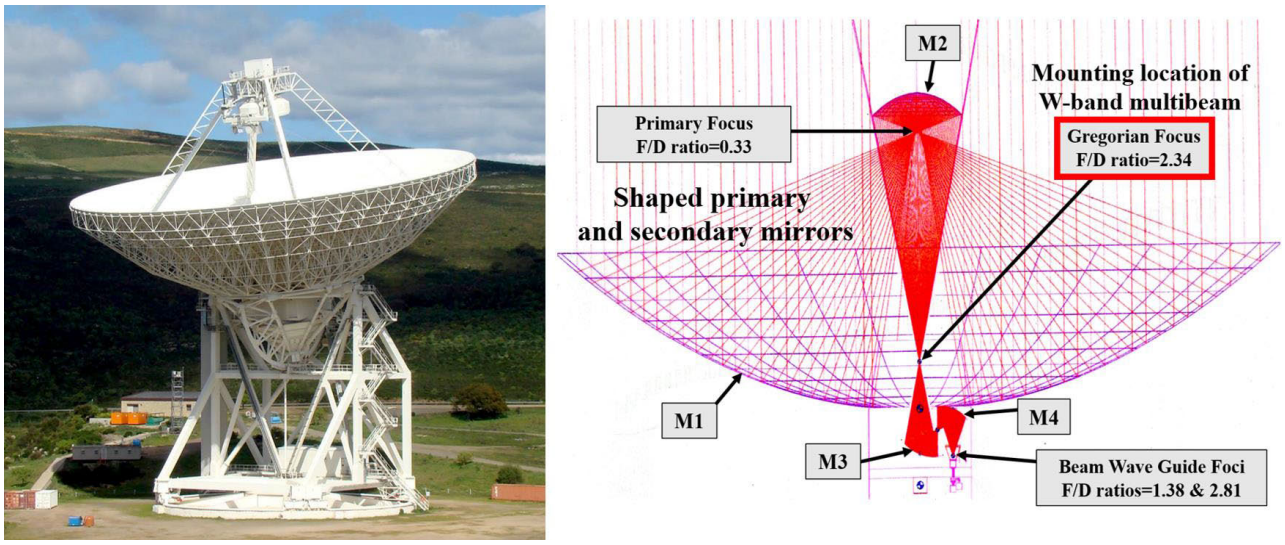

FIGURE 1. Left: Picture of the Sardinia Radio Telescope (SRT). Right: Optical configuration and ray tracing of the SRT showing the 64-m diameter primary (M1), the 7.9-m secondary (M2), and two additional Beam Waveguide (BWG) mirrors (M3 and M4). The primary and Gregorian focal positions, as long as one of four possible BWG focal positions are shown together with corresponding focal ratios. The mounting location of the W-band multibeam receiver is at the Gregorian focus ($f_2/D = 2.34$).

Large Baseline Interferometry) networks. The SRT operates as an international facility, with regular worldwide distributed calls for proposal, and no *a priori* limitation based on the affiliation of the proposers. A large fraction of the observing time (of the order of 80%) is devoted to radio astronomy applications, while 20% of the time is allocated to activities of interest to ASI, i.e. space applications and the follow-up of space science missions. The telescope is located 35 km north of Cagliari (Lat. 39°29'34'' N – Long. 9° 14'42'' E), on the island of Sardinia, Italy, at ≈600 m elevation above sea level. Its official inauguration took place in September 2013. Following a six-month Early Science Program (ESP) carried out in 2016 and a refurbishment of its active surface, the antenna (Fig. 1) has been open for scientific observation to the international community since December 2018. The SRT is carrying out radio astronomy observing programs using an initial set of receivers covering four RF bands across 0.3 − 26.5 GHz [5]–[9] and operates in single-dish (continuum, spectral lines, spectro-polarimetry, and pulsar) and VLBI modes. The telescope has been successfully used for solar observations [10] as well as for monitoring and tracking space debris [11].

The high profile of the first scientific publications have confirmed the entry of SRT in the international context and have demonstrated the capabilities of the antenna to operate as a single dish and in interferometric modes (http://www.srt.inaf.it/astronomers/science_srt/). Additional details with updated information on the SRT and the other INAF radio telescopes can be found at the following web page: https://www.radiotelescopes.inaf.it/.

The aim of this paper is to present the science drivers and the feasibility study for a low-noise broad-band heterodyne W-band multibeam receiver for the SRT. Once equipped with such a receiver, the SRT will be one of the few large single-dish radio telescopes in the world capable of carrying out high-sensitivity spectral line and continuum mapping across the 3 mm atmospheric window.

A. SRT DESIGN

The telescope optical design is based on a quasi-Gregorian configuration with shaped 64-m diameter primary (M1) and shaped 7.9-m diameter secondary (M2) reflectors to minimize spillover and standing waves (Fig. 1). Table 1 shows the main optical specifications of the SRT.

The telescope is designed to host up to 20 receivers in six focal positions that can be selected through robotic systems: Primary focus (F1), Gregorian focus (F2), and Beam-Wave-Guide foci (F3&F4 and F5&F6), with focal length to diameter ratio (f/D) (and frequency range) equal to 0.33 (0.3-20 GHz), 2.34 (7.5−116 GHz), and 1.38& 2.81 (1.4−35 GHz), respectively. The W-band receiver will be installed at the Gregorian focus, with $f_2/D = 2.34$. The taper angle, i.e. the half angle subtended by the edge of the sub-reflector with respect to the optical axis, as seen from the Gregorian focus, is 12 deg.

The primary mirror M1 utilizes an active surface with 1008 aluminum panels and 1116 electromechanical actuators to compensate for the gravitational deformation in quasi-real-time and is continuously adjusted during the observations. The actuators are also used to convert the shaped surface of the primary mirror to the ideal parabolic profile during primary focus observations. The active primary reflector panels were aligned to a surface accuracy of about 300 μm RMS (Root Mean Square) [4], compared to the ideal shaped or parabolic profile. Open-loop control of the active systems allows achieving the antenna performances needed to observe

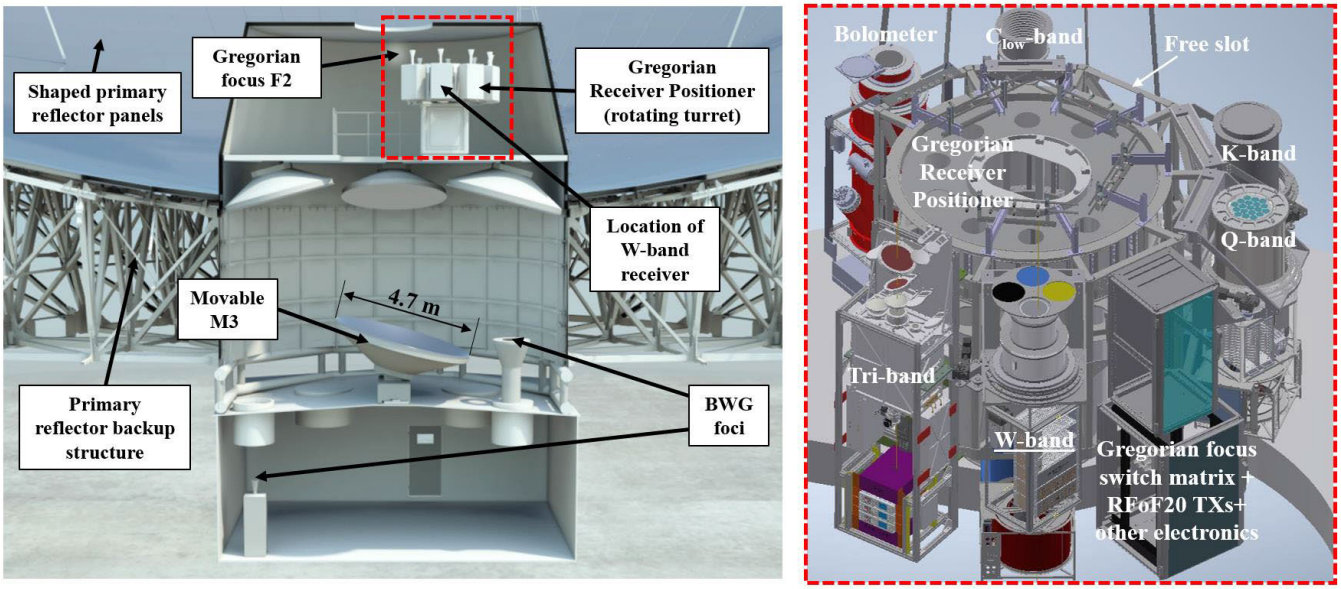

FIGURE 2. Left: Cross-section of the SRT showing the Gregorian and BWG (Beam Waveguide) receiver cabins and the position of the W-band multibeam receiver on the Gregorian Receiver Positioner (GRP, rotating turret). Right: 3D sketch with GRP slots allocated to the existing and future receivers, including the W-band multibeam, indicated as "W-band."

TABLE 1. Optical parameters of the Sardinia Radio Telescope.

Optical configuration	Shaped Gregorian
Sub reflector geometry	Numerical
Prime mirror diameter, D [m]	64.008
Sub reflector diameter, d [m]	7.9060
Focal length, f [m]	21.0236
Prime focus focal ratio, f_1/D	0.3285
Secondary focus focal ratio, f_2/D	2.342
Distance from Prime to Gregorian foci [m]	17.4676
Magnification, M [m]	7.13
Prime focus to sub reflector vertex [m]	2.8524
Secondary focus to sub reflector vertex [m]	20.3200
Secondary focus to primary dish vertex [m]	3.5560
Prime mirror vertex to aperture plane [m]	12.1415
Prime focus to aperture plane [m]	8.8821
Prime mirror half-angle [degree]	74
Sub-reflector half-angle [degree]	12

efficiently up to the maximum frequency of the currently deployed receivers, 26.5 GHz. It consists of metrological and modeling approaches that measure the deformations due only to the gravity loads at a few pointing elevations. Such deformations were evaluated by means of close-range photogrammetry (CRP) and holography measurements.

For antenna pointing, the telescope staff usually carries out routine calibration by measuring the flux of bright radio astronomical sources. Once one obtains the pointing error distribution with respect to the commanded direction, a pointing model is calculated through a least-squares fitting. The pointing accuracy of the SRT with the existing metrology system is ≈5 arcsec [4], which is adequate for K-band observations. For mapping experiments, it is important to ensure that the pointing accuracy is not affected by the scanning speed. The tracking accuracy of the SRT was tested through OTF (On-The-Fly) scans, an observing technique where the telescope continuously scans along a row or column with a given velocity instead of tracking individual points. It was verified that the pointing accuracy along the tracking axis is stable at the sub-arcsec level for any scanning speed [3]. The required pointing accuracy for any single-dish telescope is generally expressed as $\theta_{\mathrm{RMS}} < 0.1$ HPBW (Half Power Beam Width). At 100 GHz, where the SRT HPBW is ≈12 arcsec, the specified RMS accuracy is $\theta_{\mathrm{RMS}} < 1.2$ arcsec. We plan to achieve this pointing accuracy by implementing a closed-loop control that iterates measured/corrections of the gravitational and thermal effects on the antenna primary dish structure and the secondary mirror M2. The new SRT metrology system with closed-loop control has been designed in the framework of the SRT upgrade program, the PON grant (PON OR5), to be discussed in the next sub-section. This new metrology system will monitor and control the structural deformations affecting the pointing and aperture efficiency and will improve the RMS surface accuracy to ≈150 μm, required for high-efficiency observations in W-band (corresponding to ≈$\lambda/20$).

Extensive atmospheric monitoring of the SRT site and the models employed to estimate the attenuation and variability of the signal due to the atmosphere have demonstrated that it will be possible to carry out radio astronomical observations across the 3 mm atmospheric window available from the ≈600 m altitude SRT site for a good fraction of the operating time, mainly during the winter season. In particular,

TABLE 2. SRT Receivers: The W-Band 4 × 4 multibeam heterodyne receiver (pon or1) is among those under construction.

Receiver	Frequency range [GHz]	Beams x polarizations	IF BW per RFoF link [GHz]	Polarization type	Focal position	Status
Dual frequency L-P band coaxial feed	0.305-0.410 1.3-1.8	1 × 2 1 × 2	0.105 0.5	H/V or L/R H/V or L/R	Primary	Operational Operational
C_{high} band	5.7-7.7	1 × 2	2.0	L/R	Beam Waveguide	Operational
K band (extended)	18-26.5	7 × 2	2.0 (8.0)	L/R	Gregorian	Operational
S band	3.0-4.5	7 × 2	1.5	H/V	Primary	Under construction
C_{low} band	4.2-5.6	1 × 2	1.4	L/R	Gregorian	Under construction
Q band	33-50	19 × 2	16	L/R	Gregorian	PON OR2
W-band	70-116	16 × 2	8	H/V	Gregorian	PON OR1
Tri-band (K/Q/W)	18-26 / 34-50/ 80-116	1 × 2	8 / 16 / 16	L/R	Gregorian	PON OR4
W-band KID detector bolometer	≈77-103	408	-	Polarization insensitive	Gregorian	PON OR3

50 years of radiosonde profiles data measured daily at the Cagliari airport (≈30 km far, at sea level), scaled for the SRT site, show that the value of Precipitable Water Vapor is PWV $<$ 11 mm (50^{th} percentile) and the opacity is $\tau <$ 0.2 (50^{th} percentile) at 100 GHz [12]. Estimation of sky opacity, based on recorded atmospheric data, forecasts $\tau <$ 0.15 (50^{th} percentile) at 93 GHz during winter nights. The PWV in the same conditions is about 8 mm [13]. Estimates of the SSB (Single Side Band) system noise temperature referred to the receiver input, $T_{sys,SSB}$, were derived with the program described in [13], which utilizes a molecular absorption model and allows to predict it several hours before the astronomical observation, therefore offering the possibility of dynamic scheduling. The predicted system noise temperature $T_{sys,SSB}$ (at 90 deg elevation angle) has broad minima in the range 85−105 GHz and achieves values of order 100 K or lower during winter [14], having assumed a receiver noise $T_{rec,SSB} = 60$ K, based on expected instrument performance (to be discussed in detail in the following sections). In the winter, there is a 30–33% probability of finding 100 GHz opacity below 0.15 Np, which allows roughly 40 days of very good observations at that frequency. The SRT antenna gain is expected to vary from 0.50 to 0.70 K/Jy for the frequency range 0.3–50 GHz and to be about 0.34 K/Jy across the 3 mm band [4].

B. SRT UPGRADE PROGRAM AND PON GRANT

The SRT telescope is currently equipped with three cryogenic front-ends, covering four bands: P-band (305−410 MHz), L-band (1.3−1.8 GHz), high C-band (5.7−7.7 GHz), and K-band (18−26.5 GHz). So far, no scientific observations have been conducted with the SRT across the 3 mm atmospheric window. One of the initial INAF goals for the upgrade of the current set of SRT front-ends aimed at constructing a prototype W-band single-pixel receiver [15]–[17] to test the telescope active surface [18] and the metrology system to demonstrate observation capabilities up to the antenna highest design frequency (≈100 GHz). Thus, a W-band single-pixel receiver prototype was adapted and characterized in the laboratory. However, the installation of the prototype in the antenna was not finalized since in the meantime the Italian Ministry of University and Research funded the major INAF proposal for the SRT upgrade, known as the PON grant (National Operational Program), which included the development of a high-performance W-band multibeam receiver "PON OR1" (PON "Obiettivo Realizzativo" n. 1, or Work Package n. 1) [19], whose feasibility study is described with details in this article. The PON grant aims at upgrading the SRT and at extending its current capabilities to higher frequencies (>26.5 GHz), as discussed in [20]. Besides to the W-band receiver (PON OR1), eight other undergoing upgrades are also included (not yet operational): a 19-beam cryogenic receiver in Q-band (PON OR2); a W-band KID (Kinetic Inductance Detector) bolometric camera (PON OR3); a triple-band K-Q-W simultaneous receiver for VLBI (PON OR4); a new metrology system (PON OR5); new generation backends (PON OR6); new electronic and mechanical interfaces for the integration of the new systems (PON OR7); new HPC (High-Performance Computing) and storage systems for the archival and use of SRT data (PON OR8); new laboratory instrumentation for the development of microwave and mm-wave technologies for SRT (PON OR9). At the time of writing, all PON work packages are underway and the receivers are under construction.

TABLE 3. W-band multibeam heterodyne receivers in the international context.

Telescope	Diameter [m]	RF band [GHz]	IF bandwidth [GHz]	N. of pixel	N. of polar	$T_{rec,SSB}$ [K]	Notes	Ref.
SRT, Italy	64	70-116	8+8	16	2	60*	-	This work
GBT, USA	100	85-116	1.5+1.5	16	1	40-80	ARGUS	[22]
LMT, Mexico	50	85-115.5	15	16	1	55-90	SEQUOIA	[23]
TRAO, Korea	14	85-115.5	15	16	1	150-400	SEQUOIA second pol.	-
NRO, Japan	45	80-116	8+8	4	2	30-70	FOREST	[24] [25]

*Expected SSB receiver noise performance.

A summary of the SRT receivers is given in Table 2, while a preliminary 3D sketch of the instruments to be located at the Gregorian focus is shown in Fig. 2.

The preliminary design concept of the 4 × 4 W-band multibeam heterodyne receiver was carried out by INAF and included as a baseline design in the framework of the PON OR1 call for tender. INAF awarded the contract for the realization of the W-band receiver array to UKRI (UK Research and Innovation) after a pre-selection and competitive dialogues with the applicants, i.e. a co-engineering work, that allowed them to finalize the technical solutions and instrument specifications based on the allocated bid price and schedule.

In this paper, we discuss the scientific motivations for upgrading the SRT with the W-band focal plane array receiver and report on an advanced feasibility study of the instrument that would fulfil its preliminary requirements. The W-band receiver will utilize the Monitor and Control (M&C) unit and the build-to-print mechanical derotator developed by INAF. The INAF front-end design concepts as well as the definition of the interfaces described in this manuscript (optical, electrical, mechanical, etc.) are the result of a long-term effort that allowed to establish the necessary elements for the final instrument development that has been entrusted to the selected supplier (UKRI). The advanced feasibility study provides some details of its main sub-systems, as they were presented in the call for bid documentation: the optics, the cryogenic modules, the down-conversion modules, the cryostat, the solar filtering system, the mechanical derotator, the M&C unit. We discuss the advantages and disadvantages of each of the proposed solutions and describe the constraints and interfaces of the receiver inside the SRT Gregorian antenna focal cabin.

C. W-BAND ARRAY FOR THE SRT IN THE INTERNATIONAL CONTEXT

The basic layout proposed for this receiver, consisting of at least nine beams with a goal of 16 beams, will outperform all equivalent instruments currently operating on other radio astronomy facilities in terms of expected spectral configurations, polarization capabilities, and instantaneous bandwidth, until new generation instruments will become available at those facilities (see for example [21]). In particular, the 70−116 GHz multibeam receiver for the SRT will be based on cryogenically cooled low noise preamplifiers and sideband separating down-converters. The instrument will offer a variety of observing modes, including dual-linear polarization and dual-sideband, with expected noise performance of less than $T_{\mathrm{rec,SSB}} = 60$ K. Unlike other equivalent instruments, the array footprint on the sky will not rotate as the elevation angle changes during source tracking, as the SRT receiver will be equipped with a mechanical derotator. The front-end will be a very valuable complement to equivalent instruments already installed on other telescopes, as given in Tab. 3, and described in [22]–[25]. For a more detailed review of radio astronomy receivers in the international context see [26].

The W-band SRT receiver will observe two polarizations at the same time over a broad instantaneous bandwidth, which will allow the SRT to fill an existing observational gap that will benefit the entire international scientific community.

D. IF SIGNAL TRANSPORTATION AND INTEGRATION OF RECEIVERS

Fig. 3 shows a block diagram of the planned overall SRT signal transportation and processing and includes three of the future Gregorian focus high-frequency heterodyne receivers, the W-band, the Q-band and the tri-band, as well as the already operating K-band, which will be upgraded to cover wider IF bands. These four Gregorian focus receivers must be integrated with the ones already operational and must be operated through a common interface that allows their remote control, as described in [27]. In particular, as observations will be carried out using one instrument at the time, the "Gregorian Focus Switch Matrix" (represented by a large yellow box in Fig. 3) will switch among receivers to select which receiver's IF outputs are sent to the remote backends. As it will be clarified in the next sections, the W-band 4 × 4 multibeam (represented by the blue box) will deliver

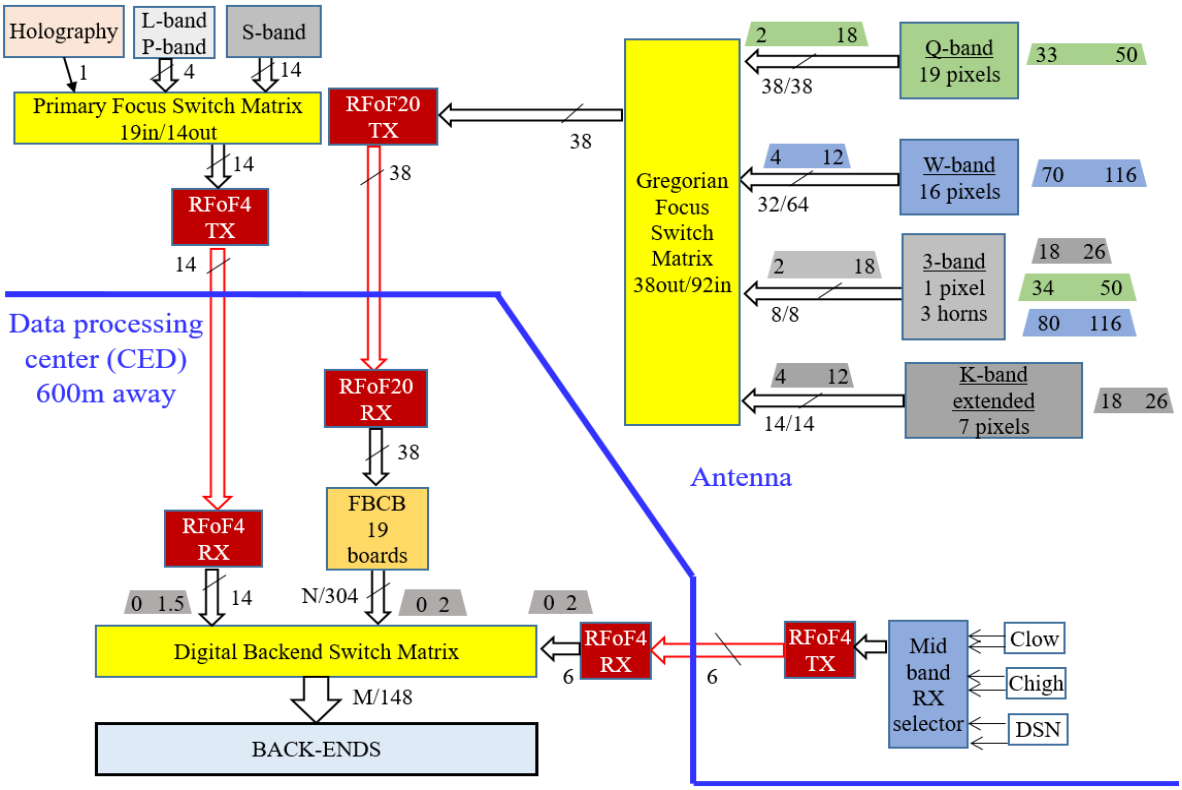

FIGURE 3. Block diagram of the distribution of the IF signals from the SRT receivers (at different focus locations) to the data processing center backend room. The high-frequency receivers in the Gregorian focus are depicted by colored boxes on the top right. The 4 × 4 W-band receiver, represented by the blue box, delivers 32 IF outputs. The IF outputs of all high-frequency heterodyne receivers are linked to the Gregorian focus switch matrix, represented by the large yellow color box. After selection by the Gregorian focus switch matrix the 32 × (4 − 12 GHz) IF signals from the 4 × 4 W band receiver are routed to 20 GHz bandwidth analog RFoF fiber optics links, referred to as RFoF20.

32 × 8 GHz-wide IF output signals through the signal transportation system. A huge amount of bandwidths must be managed by such a system, totaling 1088 GHz of IF bandwidth for the four high-frequency receivers: 608 GHz from the 19-beam Q-band (19 × 2 pols × 16 GHz), 256 GHz from the 16-beam W-band (16 × 2 IFs × 8 GHz), 112 GHz from the simultaneous tri-band (1 × 2 pols × 8 GHz + 1 × 2 pols × 16 GHz + 1 × 2 pols × 2 IFs × 16 GHz), and 112 GHz from the extended 7-beam K-band (7 × 2 pols × 8 GHz). As shown in Fig. 3, the Gregorian focus switch matrix will have 92 × IF inputs and a number of IF outputs limited to a maximum of 38 signals. The 38 selected outputs are routed to 38 analog RFoF (Radio Frequency over Fiber) optics links with 20 GHz bandwidth (indicated as RFoF20). The switch matrix and the RFoF20 optical transmitters will be installed at the Gregorian receiver positioner, while the RFoF20 optical receivers will be installed in the data processing center (CED), approximately 600 m away from the antenna, close to the SRT control room.

The number of 4−12 GHz IF outputs of the 4 × 4 W-band multibeam receiver is halved from 64 (the total number available at the output of the down-converters) to 32 (available at the receiver output interface) by an internal IF selector (not shown in Fig. 3) for compliance with the number of available RFoF20 optical links (38 plus two spares). The IF signals selected by the Gregorian focus switch matrix, transported through the RFoF20 optics links, are sent to a second down-converter named FBCB (Full Band Conversion/Continuum Board/Backend), represented in Fig. 3 by a dark yellow box. The FBCB, based on 19 boards, divides the full 16 GHz IF bands (2−18 GHz) from some of the selected high-frequency receiver into 8 × 2 GHz-wide sub-bands. The FBCB has 38 inputs and delivers 304 (38 × 8) outputs across 0.1−1.9 GHz. It incorporates analog total power full-Stokes detection for the 304 × 2 GHz-bandwidth signals. In the data processing center, cascaded with the FBCB, a digital backend switch matrix will connect the desired receiver outputs to the desired backends. A selection of the 304 × 2 GHz-wide sub-band signals from the FBCB will be connected and processed by a variety of backends. These include digital wideband and high-resolution backends based on: 1) Xilinx Virtex-7 FPGA-based Square Kilometer Array Reconfigurable Application Board (SKARAB) [28]; 2) new Radio Frequency System on Chip (RFSoC) technology [29]; 3) DBBC3 (version 3 of Digital BaseBand Converter) [30]; 4) digital filter bank, ROACH-1 (version 1 of Reconfigurable Open Architecture Computing Hardware) [31]; 5) SARDARA (SArdinia Roach2-based Digital Architecture for Radio

Astronomy) spectropolarimeter backend [32]; 6) SETI (Search for Extraterrestrial Intelligence) Breakthrough Listen program backend [33]; 7) space debris backend [34]; 8) Deep Space Network (DSN) backend [35], [36]; 9) holography backend [37]; 10) RFI (Radio Frequency Interference) backend [38] and spectrum analyzer backend. The SKARAB, RFSoC and DBBC3 backends are currently under development within the PON OR6 upgrade program, while all the others are already commissioned and operational at the telescope. See also http://www.srt.inaf.it/project/backends/ and [3] for further details.

E. OBSERVING MODES

The W-band multibeam will produce 128 × 2 GHz-wide sub-bands at the FBCB outputs. Not all sub-bands can be delivered to the digital backends. The outputs will be selected to enable various observing modes, which will include the following ones:

a) Observing mode with 16 dual-polarization feeds: only one 2 GHz-wide sub-band, selected between 4−6 GHz, 6−8 GHz, 8−10 GHz, or 10−12 GHz, will be routed and processed for each of the 32 sub-bands transmitted by the FBCB (a total of 64 GHz of bandwidth will be processed by the digital backends);
b) Observing mode with 10 dual-polarization feeds: two interlaced sub-bands at choice, either 4−6 GHz & 8−10 GHz or 6−8 GHz &10−12 GHz will be routed and processed by the digital backends;
c) Observing mode with two dual-polarization feeds: all four sub-bands, 8 GHz wide, will be routed and processed by the digital backends, for a total of 32 GHz instantaneous band.

As it will be clarified in Sec. IV, our proposed W-band receiver architecture allows simultaneous observation of both H and V polarizations of either the Lower Side Band (LSB) or the Upper Side Band (USB), or of both LSB and USB of either H or V, for the above listed feeds/sub-bands combinations. All pixels of the array will track the same frequency window, so nominally a single spectral region is observed by the array.

II. SCIENCE DRIVERS FOR THE W-BAND MULTIBEAM RECEIVER ON THE SRT

A 3 mm band heterodyne multibeam receiver operating on the SRT is an extremely valuable resource for many applications in both galactic and extragalactic astrophysics. The large collecting area of the SRT (≈3200 m^2) combined with the large angular coverage offered by the W-band array will allow fast mapping of extended low-brightness sources with an angular resolution of ≈12 arcsec. The receiver will be available to the general radio astronomy community and will enable simultaneous observation of continuum emission and spectral lines, using both total power backend and the high-spectral resolution digital backends previously mentioned. The wide instantaneous IF bandwidths of the receiver (goal 8 GHz per sideband) will reduce the mapping time during spectral imaging of extended sources and during spectral surveys. For example, the ^{12}CO(1-0) and the ^{13}CO(1-0) lines with rest frequencies of 115.3 GHz and 110.2 GHz, respectively, corresponding to a frequency separation of ≈5.1 GHz, can be observed in a single LO receiver tuning. The receiver will be capable of covering the observation of the 70−116 GHz frequency band with four LO frequency tunings, and of most of the 75−116 GHz band, which has over 2,000 detected molecular lines [39] with only three LO frequency tunings. A short and preliminary list of the main instrument science drivers is provided below:

a) Multi-spectral line observations of both compact and diffuse low-temperature molecular gas typical of the interstellar medium and of star-forming regions. The mapping of molecular species such as HCO+/HCN/HNC, SiO, CH3OH, CS, and their isotopologues will allow studying the kinematics and the chemistry of these regions [40]. In particular, in recent years star-formation studies have concentrated on the modeling and observations of the molecular ''filaments'', which SRT will be able to map with a linear resolution similar to their typical width, i.e., ∼0.1 pc. It is also possible to study the so-called interstellar ''bubbles'' detected at infrared wavelengths to better understand the physical processes that generate them.
b) Simultaneous observation of various molecular gas tracers to advance the study of star formation in nearby galaxies, by analyzing the relationship of the most abundant gas tracer (e.g., CO, HCO+, HCN, HNC) to other signposts of star formation. W-band observations will also allow correlating star formation rates in different types of galaxies with the abundance of CO, HCN, and other molecular tracers. The wide instantaneous receiver frequency range and the new digital spectrometer will also allow detecting the ^{12}CO(1-0) and the ^{13}CO(1-0) line transitions in high-redshift galaxies [41];
c) Mapping of the radio emission from the Sun and use of these observations for Space Weather applications. Recent advances in single-dish solar imaging are provided up to 26 GHz by the INAF radio telescopes in the frame of the SunDish project [10], [42], [43] (see https://sites.google.com/inaf.it/sundish for details). The SunDish system can presently offer solar observations with a relatively coarse resolution (1 arcmin) with respect to typical size of the solar disk features. Multi-pixel W-band observations will provide excellent spatial resolution and will achieve unprecedented details for solar radio monitoring, thus expanding the potentialities of the imaging techniques of the SunDish system. No regular solar monitoring at 100 GHz is presently available from the ground. This frequency band can offer a clear and unprecedented picture of both thermal and non-thermal (gyro-synchrotron emission) evolution of the active Sun, useful for Space Weather forecast.

The atmospheric opacity fluctuations in W-band require relatively short observing time to optimize the calibration process and the scientific results in terms of observing parameters (sensitivity and reduction of systematic effects due to atmospheric variability during the observation). The W-band multibeam receiver will allow performing high-spatial-resolution surveys in regions of the sky with an angular size of a few arcminutes in a relatively short observing time. The instantaneous FoV covered by the 4×4 array will be $\approx 2.3 \times 2.3$ arcmin^2, unfilled, with separation between contiguous elements of 43 arcsec. The operational parameters of the receiver will be determined during its scientific validation phase through specific observing campaigns aiming at establishing the observational performance of the instrument.

A convenient parameter to express the sensitivity of the antenna and receiver overall sensitivity is the System Equivalent Flux Density (SEFD), defined as the ratio between the overall system noise temperature $T_{\mathrm{sys,SSB}}$ (including receiver noise temperature and the atmospheric contribution) in degrees Kelvin and the antenna gain Γ in Kelvin/Jansky (K/Jy) given by $\Gamma = \eta_{\mathrm{eff}} \pi D^2/(8k_{\mathrm{B}})$, where η_{eff} is the antenna efficiency, D is the diameter of the antenna, $k_{\mathrm{B}} = 1.38\ 10^{-23}$ m^2 kg s^{-2} K^{-1} is the Boltzmann constant, and 1 Jy $= 10^{-26}$ W m^{-2} Hz^{-1}. Assuming a receiver noise temperature $T_{\mathrm{rec,SSB}} = 60$ K, a system temperature $T_{\mathrm{sys,SSB}} \approx 135$ K at an elevation of 45 degrees, and an aperture efficiency of $\eta_{\mathrm{eff}} \approx 0.7$ at a frequency of 93 GHz, one gets $SEFD = T_{\mathrm{sys,SSB}}/\Gamma \approx 165$ Jy, where $\Gamma \approx 0.82$ K/Jy. A value of SEFD ≈ 530 Jy would be obtained with non-optimum atmospheric conditions for an off-axis feed, near the RF band edges. The RMS uncertainty in Jy when observing in a frequency band $\Delta\nu$, with an integration time Δt can then be easily calculated as $\mathrm{SEFD}/\sqrt{\Delta\nu\Delta t}$.

The availability of multi-feed receivers, such as the instrument described in this work, makes the SRT a fast mapping telescope. All standard observing modes are supported, including raster scans and OTF mapping in the equatorial, galactic, and horizontal coordinate frames. An estimate of the mapping speed of the SRT for various array sizes was given in [44]. After updating the atmospheric and receiver parameters used in [44], the total observing time required to map a 10×10 arcmin^2 region with the 4×4 W-band array (in position switching mode), at a 0.1 K sensitivity level and using a 0.25 MHz resolution bandwidth, is about 2 hr.

III. TOP-LEVEL SPECIFICATIONS OF THE W-BAND MULTIBEAM RECEIVER ON THE SRT

The main specifications of the W-band receiver, including the instrument minimum requirements and the goal requirements, are given in Table 4. The front-end must be capable to observe weak radio astronomy sources with high sensitivity but also the strong signals from the Sun without saturating the receiver chains. The heterodyne array receiver will be based on a cryogenic module comprising dual-polarization pixels consisting of a cascade of feed-horn, OMT and High Electron Mobility Transistor (HEMT) W-band LNAs cryogenically cooled at $\approx$20 K by a close-cycle refrigerator. In particular, the $\approx$20 K HEMT amplifier technology is favored in comparison to the $\approx$4 K Superconductor-Insulator-Superconductor (SIS) mixer technology that offers similar noise performance across W-band. The array shall have a minimum of nine feeds in a 3×3 configuration capable of high-efficiency illumination of the antenna. Based on the performance analysis carried out by [44] our goal is an array of 16 feeds in a 4×4 configuration covering the 70−116 GHz band with a down-converter delivering 16 GHz of sky frequency per polarization. The down-converter can utilize either a dual Sideband Separation (2SB) mixing scheme, delivering two 8 GHz IF outputs, or a SSB scheme, delivering a single 16 GHz IF output (per pixel and per polarization channel).

TABLE 4. Top level requirements of the W-band multibeam heterodyne receiver for the Gregorian focus of the SRT. Both the minimum requirements and the goal requirements are listed.

RF band	Minimum 75-116 GHz. Goal 70-116 GHz
Polarization properties	Two orthogonal linear polarizations with OMTs
Number of pixels, array configuration and beam spacing	Minimum 9 pixels. Goal: 16 pixels in square 4×4 configuration. Separation between projected beams in the range 2-5.7 × HPBW at all frequencies
Antenna efficiency	$\eta_{\mathrm{eff}}=\eta_{\mathrm{t}}\,\eta_{\mathrm{s}}\,\eta_{\mathrm{p}} \geq 0.50$ across the full RF band for all feeds
Technology	Cryogenically cooled HEMT LNAs
Down-conversion scheme and IF band	2SB Mixers covering minimum 12 GHz of sky frequency per polarization. Goal 16 GHz: 8 GHz USB and 8 GHz LSB across 4-12 GHz. Alternative SSB scheme possible.
Maximum number of IF outputs	No more than 38 (limited by the number of IF signals that can be transported to the backends). A 4×4 2SB array must halve the 64×IF outputs and select 32 signals for delivery to the backends
Mechanical derotator	Yes, to track the parallactic angle
Array calibration	Single 293 K calibration load
Solar observations	Yes, with switchable filter/attenuator placed in front of vacuum window
SSB noise temperature	$T_{\mathrm{rec,SSB}} \leq 60$ K over 80% of RF band
Image band suppression	$\mathrm{R_i} \geq 10$ dB
Local Oscillator signal	Tunable via high phase stability synthesizers or YIG oscillator
Overall diameter (mm)	< 800
Height (mm)	≤2465
CTI cryocooler	Two cryogenic stages delivering ≤80 K and ≤20 K

The required SSB receiver noise is $T_{\mathrm{rec,SSB}} \leq 60$ K over 80% of RF band and the image sideband rejection $R_{\mathrm{i}} \geq 10$ dB, where the SSB noise is obtained by correcting the measured Double Side Band (DSB) noise temperature

for the image contribution to the IF output: $T_{\mathrm{rec,SSB}} = T_{\mathrm{rec,DSB}}\,(1 + 1/R_{\mathrm{i}})$. In this formula, the image sideband rejection is expressed in linear scale.

The receiver must be designed to provide high mapping efficiency by optimizing the geometry and the separation between the projected beams on the sky: the feed-dependent component of the antenna efficiency η_{eff} of the SRT antenna illuminated by all feeds, including the ones with the largest offset from the optical axis, shall be no less than 0.50 (50%) at all frequencies across the full RF band, i.e. $\eta_{\mathrm{eff}} = \eta_{\mathrm{t}}\,\eta_{\mathrm{s}}\eta_{\mathrm{p}} \geq 0.50$. The feed-horn illumination, in particular its edge taper, must be optimized accordingly. In the above formula, η_{eff} is the product of taper efficiency η_{t}, spillover efficiency η_{s}, and polarization efficiency η_{p}, while the other contributions, e.g. Ruze RMS surface errors, focus, radiation efficiency, and blockage, are not considered [45], [46], i.e. we assume they have unitary value. This assumption allows to simplify the evaluation of the performance of the receiver optical system and the verification of the compliance with the specifications, which do not depend on focus efficiency or antenna surface error parameters. If we account for all the contributions, the total antenna efficiency η_{eff} can be less than 0.5, as its frequency-dependent value depends on all factors, including the RMS phase errors that will be achieved after the upgrade of the SRT metrology system. In particular, the efficiency η_{surf} associated to the RMS surface error σ_{rms}, $\eta_{\mathrm{surf}} = exp[-(4\pi\sigma_{\mathrm{rms}}/\lambda)^2]$, depends strongly on the ratio $\lambda/\sigma_{\mathrm{rms}}$. For example, if $\sigma_{\mathrm{rms}} = 0.15$ mm, $\eta_{\mathrm{surf}}(100\ \mathrm{GHz}) = 0.67$ and $\eta_{\mathrm{surf}}(116\ \mathrm{GHz}) = 0.59$, while if $\sigma_{\mathrm{rms}} = 0.175$ mm, $\eta_{\mathrm{surf}}(116\ \mathrm{GHz}) = 0.44$. In a realistic scenario, the total antenna efficiency η_{eff} depends on all multiplicative factors, including the efficiency due to the Ruze phase errors η_{surf}.

The ratio between beam spacing and HPBW must be in the range 2-5.7 at all frequencies. The specification on the maximum value of this ratio, 5.7, is set by considerations on mapping efficiency of radio astronomy sources that are not too extended, and on the maximum number of on-the-fly (OTF) sub-scans required to cover a given region of the sky. The receiver includes a calibration system with at least one room temperature (≈293 K) calibration load and a cabinet with racks for biasing, monitor and control of all the cryogenic and room temperature active sub-systems.

Furthermore, the instrument includes a mechanical derotator with cable wrap to maintain the parallactic angle during source tracking, a mechanical support structure for its permanent installation in the receiver cabin and a vacuum pump with remotely controlled vacuum valve. The mechanical frame and the derotator will be build-to-print units to be fabricated according to the INAF executive mechanical drawings, similar to those already adopted on the K-band multibeam receiver. The W-band receiver shall be designed to allow a derotation angle (of the cryostat and of the cabinet with electronics rack to which it is bolted) of at least ± 120 °, i.e. the free rotation angle must be ≥ 240 °. No mechanical interference with receiver subassemblies (cryocooler head, vacuum pumps, cables, etc.) should limit the free rotation angle of the derotator.

The final receiver design can adopt different architectures in terms of pixel number, geometrical configuration,

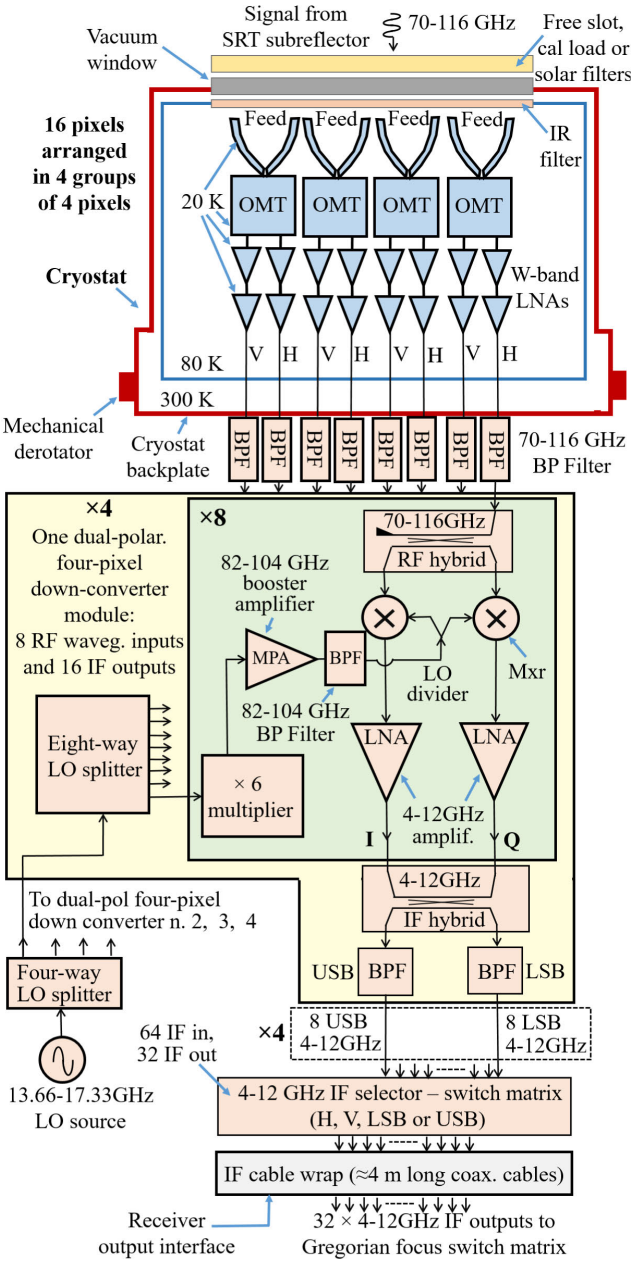

FIGURE 4. Block diagram of 70-116 GHz multibeam receiver architecture in 4 × 4 configuration showing the cryogenic components located inside the cryostat (top) and the room temperature sideband separating down-converters (center) delivering 2 × 32 IF outputs (32 USB and 32 LSB) across 4-12 GHz. Inside the cryostat, the array is organized in four rows of 1 × 4 dual-polarization receiver chains. The 4 × 4 × 2 = 32 signals at the cryostat backplate are filtered (by 70-116 GHz waveguide bandpass filters indicated as "BPF") and injected into the sideband separating down-converter. The down-converter consists of four independent modules, each serving a line of four dual-polarization cryogenic pixels. The receiver includes a mechanical derotator to track the parallactic angle with associated cable wrap. The IF selector cascaded to the down-converter (bottom) halves the number of outputs and allows selection of 32 IF signals for transportation to the external Gregorian focus switch matrix.

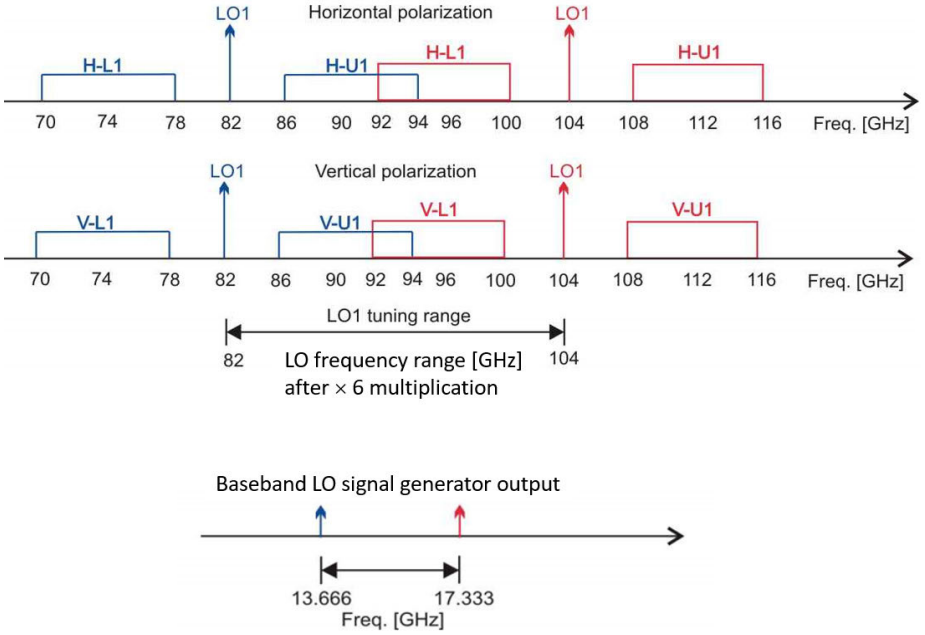

FIGURE 5. Sideband separating down-conversion scheme of the LSB (L1) and of the USB (U1) with 4-12 GHz IF (8 GHz bandwidth per sideband). Top diagram: down-converted bands with two different LO settings tuned for operations in the upper part of the 70-116 GHz band (ν_{LO} = 104 GHz, red color) and in the lower part of the lower 70-116 GHz band (ν_{LO} = 82 GHz, blue color). Both the H and V polarizations are shown along with a diagram of the fundamental LO1 tuning range at the sextupler output, 82-104 GHz. Bottom diagram: local oscillator frequency tuning range of the baseband LO signal generator output (13.666-17.333 GHz). In this example, a single baseband LO signal generator is used to pump the mixers of both polarization channels and down-convert identical RF sidebands from H and V. A different arrangement based on two independent baseband LO signal generators could be adopted to down-convert different RF sidebands from H and V.

down-conversion scheme, instantaneous IF band, placement of components inside or outside the cryostat, etc. as long as it complies with the minimum set of requirements of Table 4.

The receiver components shall be capable of retaining compliant radiometric performance at differing angles of elevation, as the antenna tracks the radio astronomy source. The receiver performance shall be uniform throughout the elements of the array.

IV. ARCHITECTURE OF THE W-BAND MULTIBEAM RECEIVER PROPOSED BY INAF

In the call for bid documentation, INAF proposed alternative receiver architectures and preliminary designs for considerations by the supplier, all compliant with the previously mentioned specifications. The front-end array recommended by INAF is placed directly at the SRT Gregorian focal plane without additional re-imaging optics, and utilizes dual-linear polarization feeds, where each array element employs a cascade of 70−116 GHz corrugated feed-horn, OMT, and HEMT LNAs. In Appendix A, we provide justifications and detailed analysis of different technical solutions for a 3 × 3 array configuration, while here we focus on our goal instrument architecture based on a 4 × 4 focal plane array.

The array is cryogenically cooled at ≈20 K inside a cryostat, as shown in the block diagram of Fig. 4. Except for the pixel number and down-converter type, the architecture is similar to the one adopted for the laboratory prototype receiver developed in the framework of WP1 of the Advanced European Technologies for Heterodyne Receivers for Astronomy (AETHRA) Radionet Joint Research Activity [47]. Fig. 4 shows that the 4 × 4 RF signals enter the cryostat from an RF-transparent vacuum window followed by an IR (Infrared) filter. The 16 dual-polarization RF signals are coupled into 32 single-polarization waveguides by the 4 × 4 array feed-OMT cascade. There are no other optical components located within the signal path from the telescope secondary to the receiver feeds during weak radio-astronomy source observations. However, for solar observation and receiver calibration, free-space bandpass solar filters and a black body reference target will be respectively introduced at the receiver input, external to the cryostat, and immediately in front of the signal input vacuum window. Therefore, the design allows the three following types of measurement: *a*) array of feed-horns pointed at the cold sky (weak radio astronomy signals); *b*) array of feed-horns pointed at the Sun (strong radio astronomy signal) after insertion of Solar filters in the signal path; *c*) array of feed-horns pointed towards a room temperature (≈293 K) calibration target, to be placed in front

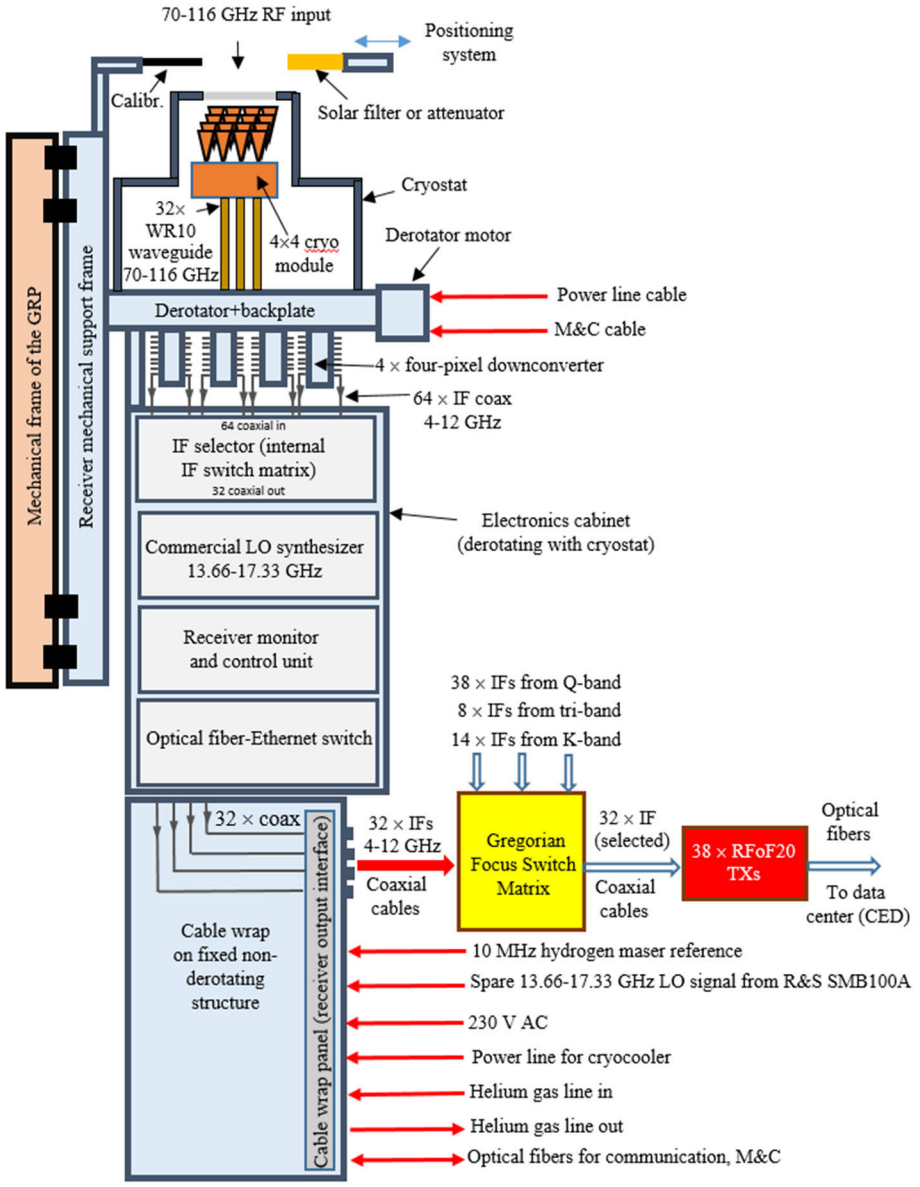

FIGURE 6. Schematic diagram of 70-116 GHz multibeam receiver (see also Fig. 4) showing the positioning system with calibrator and solar filter-attenuator, the cryostat with internal 4 × 4 cryogenic array, the four four-pixel downconverters attached to the cryostat backplate at room temperature, the derotator, the electronics cabinet (with IF selector, LO synthesizer, M&C unit and optical fiber-Ethernet switch), the cable wrap, the receiver mechanical support frame bolted to the GRP mechanical frame. This schematic illustrates the interfaces between the receiver and the infrastructure available at the SRT. The red arrows indicate the connections that will be available at the receiver cable wrap panel, which includes the interfaces for: a) 32 coaxial cables with the 4-12 GHz IF output signals (to connect to the Gregorian focus switch matrix cascaded with the 38 RFoF20 optical transmitters); b) the 10 MHz hydrogen maser reference for phase-lock of the Local Oscillator; c) the spare 13.66-17.33 GHz baseband LO signal; d) the power line for the cryocooler; e) the Helium gas supply and return lines for the cryocooler; f) the single-mode optical fibers (Tx/Rx) for the receiver M&C. The derotator motor utilizes power line and M&C cables external to the cable wrap.

of the cryostat vacuum window. Inside the cryostat, the two polarizations at each feed horn output, Pol-H and Pol-V, are separated by the OMT, amplified by the LNAs and transported from the cold front-end at ≈20 K to the warm cryostat backplate at room temperature by low-thermal conductivity waveguides.

Outside the cryostat, the 16 × 2 RF signals are band-pass filtered (BPFs) and down-converted by dual-sideband separating (2SB) heterodyne mixers operating at fundamental LO frequency (not sub-harmonic, unlike those used for AETHRA). In this 2SB receiver scheme, the RF signal of each polarization channel is mixed with a strong

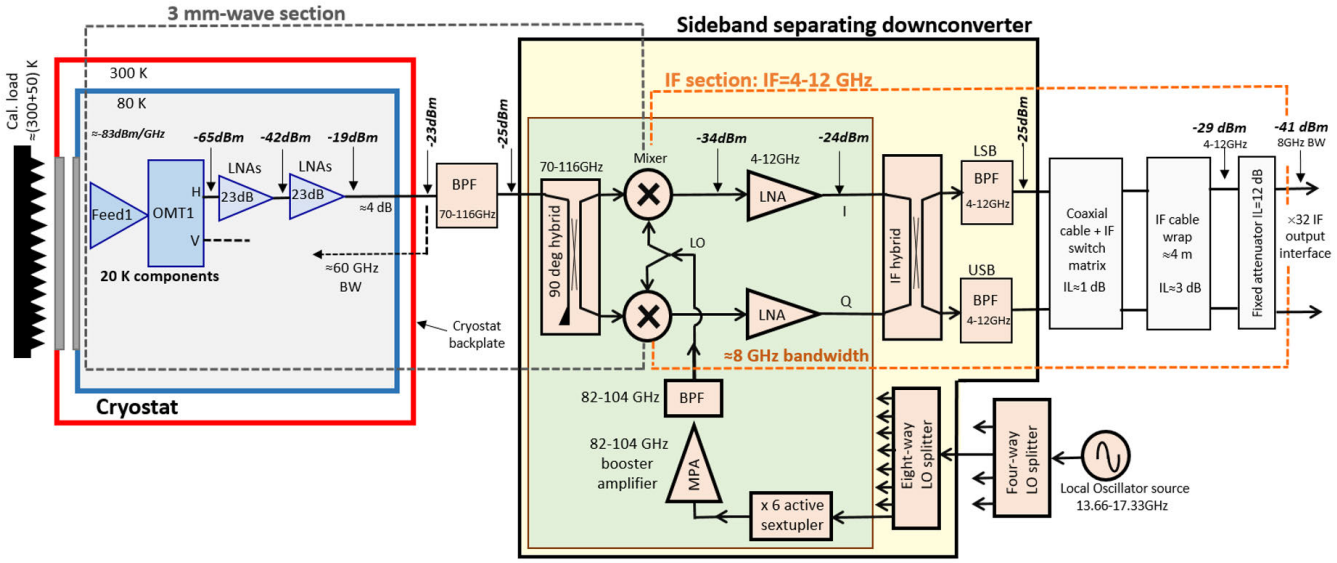

FIGURE 7. RF power budget of the W-band receiver (with architecture as in Fig. 4) looking into a ≈300 K calibration load. The target value for the output power integrated over the 4 – 12 GHz IF band (8 GHz bandwidth) of each of the 32 outputs is −41 dBm.

monochromatic signal from the tunable LO source to produce two independent IF outputs, USB and LSB, respectively $\nu_{USB} = \nu_{LO} + \nu_{IF}$ and $\nu_{LSB} = \nu_{LO} - \nu_{IF}$, both of which fall inside the 70−116 GHz frequency range. Here, ν_{LO} and ν_{IF} indicate respectively the LO and IF frequencies and it is assumed that there is no other sideband conversion from higher LO harmonics.

A schematic of the frequency conversion, showing the RF tuning range and LO frequencies is illustrated in Fig. 5. The LO system consists of a commercial low-phase-noise source generating a baseband tone across the ≈13.66-17.33 GHz frequency range, phase-locked to the 10 MHz reference signal available from the SRT Hydrogen maser, that is equally power divided via a four-way LO splitter. Fig. 4 shows that each of the four signal paths is further divided via an eight-way LO splitter and connected to a ×6 harmonic multiplier (sextupler) which increases the LO frequency to the final range, 82 GHz $\leq \nu_{LO} \leq$ 104 GHz. The multiplier output is amplified, filtered, and directed to the sideband separating mixer allowing frequency conversion. Pixel elements of the down-converters are grouped into four subassemblies (four modules of four-pixel down converters), where each down-converter of four dual-polarization pixels will have eight waveguide inputs and 16 coaxial IF outputs (8 LSB and 8 USB) operating across 4−12 GHz. The four four-pixel down-converters and the LO distribution system will be located at room temperature, outside the cryostat. In total, the down-converters will deliver 64 IF output signals across 4−12 GHz, i.e. 32 IF signals from the USB and 32 IF signals from the LSB.

However, as described in previous section, the SRT signal transportation system allows a maximum of 38 IF signals to be transported by RFoF20 optical links. Therefore, an IFs selector internal to the receiver, consisting of a switch matrix placed in cascade to the down-converters, is needed to halve the number of 64 available signals and extract 32 IFs. The IFs selector is presented in Appendix B. The IFs selector allows choosing any of the four following configurations:

- 32 × 4−12 GHz LSB (both polarizations, H and V);
- 32 × 4−12 GHz USB (both polarizations, H and V);
- 32 × 4−12 GHz of Pol-H (both sidebands, LSB and USB);
- 32 × 4−12 GHz of Pol-V (both sidebands, LSB and USB).

Only two control bits (four possible states) are required to select the desired output configuration.

We note that the basic observing modes described in the previous sub-section I-E refer to one of the four IFs selector configurations described above. Furthermore, the design leaves open the possibility to use two independent baseband LO systems, one per polarization channel, enabling observation of two orthogonal polarization bands (H and V) at different RF frequencies. Therefore, a variety of observing modes will be possible, as different combinations of feed, polarization state, and sidebands will be permitted with the W-band multibeam receiver at the SRT.

Following the internal IF selector, the 32 × IF signals will be transported by coaxial cables (≈4 m long) through the derotator IF cable wrap, up to the receiver output interface located on the cable wrap panel. A schematic of the receiver showing the interfaces (mechanical, electrical, etc.) with the antenna structure at the Gregorian focus is shown in Fig. 6.

V. RECEIVER POWER BUDGET AND NOISE BUDGET

A. RECEIVER POWER BUDGET

We refer to the sideband separating receiver architecture of Fig. 4 and provide preliminary estimates of the power and noise budgets through the receiver chain when the instrument is observing any of the following sources: *a*) the room

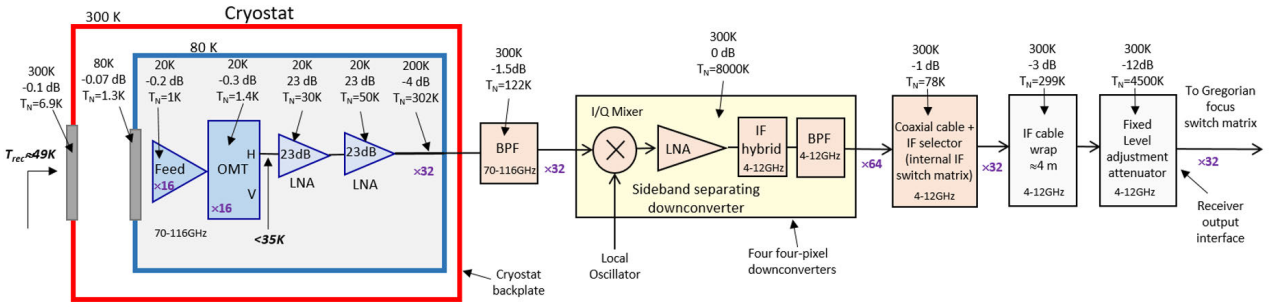

FIGURE 8. Schematic of W-band receiver with noise budget estimates (see receiver architecture of Fig. 4).

temperature calibration load; *b*) the cold sky; *c*) the Sun through solar filters.

1) RECEIVER LOOKING AT *a* ROOM TEMPERATURE CALIBRATION LOAD

Following the simplest calibration method, the receiver array will observe a single load at room temperature (≈300 K), as depicted in Fig. 7. The calibration load will be positioned in front of the receiver vacuum window. If the SSB receiver noise referred to the vacuum window is of order ≈50 K, a system noise of ≈350 K is injected into the first stage LNA. This is equivalent to system noise power density $k_B T$ ≈–83 dBm/GHz. If the input noise bandwidth is ≈60 GHz (≈60-120 GHz) the integrated power at the input of the first LNA will be ≈–65 dBm. Following two stages of amplification (≈46 dB gain) and losses due to signal transportation, the integrated power available at the cryostat backplate output will be of order −23 dBm. If the ''active'' downconverter module (cascade of sideband separating mixer and IF LNA, to be discussed in Section IX) delivers no gain, and if the insertion loss of the internal IF switch matrix and IF cable wrap with 4 m long cables is ≈3 dB, the integrated power available at the cable wrap interface would be −29 dBm (integrated over ≈8 GHz bandwidth). Fixed attenuators with value ≈12 dB could be added at the outputs for power level adjustment to achieve the total power integrated over the 4−12 GHz IF bandwidth, specified to be ≈–41 dBm. Variations of ±7 dB with respect to this target values (−48 dBm to −34 dBm) can be accepted to accommodate changes of IF output power due to non-uniformity of performance from the pixels and due to the different intensity of the observed target (from the cold sky to the Sun), while maintaining the linearity range of operations of the cascaded chain (RFoF fiber-optics links, FBCB and backends). The IF output power requirement is mainly set by the dynamic range of the RFoF links and FBCB, which integrates analog polarimeters. The alternative solution to the IF output attenuators at the receiver cable wrap output would be to adopt a down-converter design with no LNAs in its IF section.

2) RECEIVER LOOKING AT THE COLD SKY

When the receiver is coupled to the SRT optics and observes the cold sky, rather than the ≈300 K calibrator, the system noise power density injected into the first stage LNA depends on the atmospheric transparency, on the antenna elevation angle, spillover, frequency, etc. In W-band, its value is expected to vary in the range ≈100–200 K during observation [14]. With a minimum system noise at the receiver input of ≈100 K the integrated power at the output of the IF cable wrap would be of order −45 dBm.

3) RECEIVER LOOKING AT THE sUN THROUGH SOLAR FILTER

The Sun emissivity has an expected average brightness temperature of 5000-100000 K within the ≈12 arcsec HPBW W-band radio beams of the SRT, with possible sporadic emission up to 10^6 K due to bright solar flares [48], [49]. To avoid saturation of the second cryogenic LNA stage, the total RF power incoming into the receiver is reduced by ≈10 dB by quasi-optical bandpass RF solar filters (centered at 78 GHz and 110 GHz) with ≈6% relative bandwidth (bandwidth reduction from ≈60 GHz to ≈6 GHz). The integrated total power at the output of the cable wrap is of order −36 dBm (≈5 dB higher than the −41 dBm target).

If no attempt is made to filter out or attenuate the incoming RF power, the system noise power injected into the receiver will drive the last LNA stage of each pixel/polarization into saturation. A technique will be explored to de-tune the bias of the LNAs and lower their total gains, thus avoiding saturation, as described in [50]. The bias de-tuning can be performed remotely using the ''GAIA'' digital LNA bias board, which will be discussed later in Section X. A SSB receiver noise temperature $T_{\mathrm{rec,SSB}} < 1000$ K at all frequencies (70−116 GHz) is considered to be acceptable for Solar flare observations.

B. RECEIVER NOISE BUDGET

Receiver noise budget breakdown considerations (atmospheric contribution excluded) are provided for the receiver schematic of Fig. 4. The Friis formula is used to estimate the receiver noise referred to its input, which depends on the noise and gain of a cascade of stages. We assume that the two cryogenic W-band LNAs have the same gain (23 dB) and noise temperatures of 30 K and 50 K, respectively for the first and second stage modules. The noise contribution added by the passive components (vacuum window, IR filter, feedhorn, OMT, waveguide sections, BPF, coaxial cables, etc.) depends on their insertion loss and on their physical tempera-

ture. The noise of the input section in front of the LNA is the aggregate of the thermal radiation arising from small losses at various temperatures ranging from room temperature (≈300 K) down to the cryogenic operating temperature (≈15-20 K). The losses incurred at room temperature, due to the vacuum window, are the most harmful to the noise and should be minimized.

Fig. 8 shows a simplified schematic of the full receiver chain with indication of the expected noise referred to its input, resulting in a total receiver noise of $T_{\mathrm{rec,SSB}}$ ≈49 K. The values of the physical temperature of the receiver elements (300 K, 80 K or 20 K), the insertion loss, and the noise equivalent temperature of each of the elements are also indicated. These values are also listed in Table 5.

TABLE 5. Receiver noise and gain budget estimates (referred to fig.8).

Component	Noise [K]	Physical temp. [K]	Gain [dB]	Noise contr. [K]
Vacuum window	7	300	-0.1	7
Infrared filter	1.3	80	-0.07	1.3
Feed-horn	1	20	-0.2	1
OMT	1.4	20	-0.3	1.6
LNA first stage	30	20	23	36
LNA second stage	50	20	23	0.3
Signal waveguide transport	302	200	-4	0.01
70-116 BPF	123	300	-1.5	0.01
Active down-converter	8000	300	0	0.8
Coaxial cable + IF selector	78	300	-1	0.01
IF cable wrap	299	300	-3	0.04
Adjustment attenuator	4455	300	12	1.16
Total			≈24	≈49

VI. W-BAND ARRAY RECEIVER OPTICS AND CRYOGENIC MODULES

A. FIELD OF VIEW FROM THE SRT GREGORIAN FOCUS

The W-band multibeam receiver will be placed on the SRT Gregorian focus receiver positioner (GRP), a rotating platform eccentrically mounted at the Gregorian focal plane illustrated in Fig. 2. A picture of a portion of this rotating platform is shown in Fig. 9. The GRP has a decagonal shape and will host up to eight different cryogenic receivers for operation over a range of frequencies from 4.2 GHz to 116 GHz. A drive system can rotate the turret so that any of the receivers can be positioned on the optical axis of the telescope. The maximum dimensions of the W-band receiver in the vertical direction (parallel to the optical axis) is 2465 mm. The overall size and weight of the instrument are expected to be similar to the K-band multibeam receiver developed by INAF [7], also visible in Fig. 9.

The receiver optics provides high mapping efficiency by optimization of the geometry and the separation between

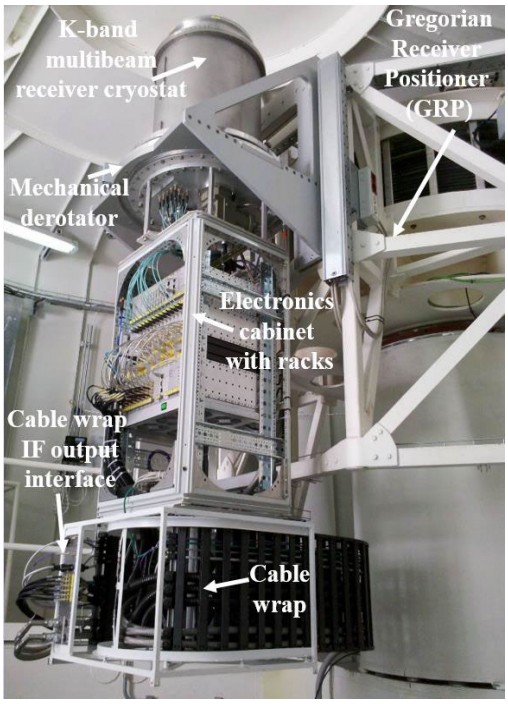

FIGURE 9. Picture of the GRP rotating platform supporting the receiver(s), with K-band receiver in focus position.

the projected beams on the sky. As the minimum element spacing of any array in the Gregorian focal plane that efficiently illuminates the antenna corresponds to an angular spacing on the sky equal to almost twice the HPBW of the antenna, the FoV cannot be fully sampled [51]. For large-area mapping it is desirable to achieve the smallest possible separation between the projected beams in the sky, of about 2 HPBW (see Table 4), where HPBW is wavelength and illumination dependent and of order $1.22\,\lambda/D$. For $\lambda = 3$mm ($\nu = 100$ GHz), $D = 64$ m, HPBW≈11 arcsec. Different receiver architectures and cryogenic array configurations can achieve the required high-efficiency SRT illumination and beam spacing specified in Table 4, including the following:

- re-imaging optics in front of the array;
- non-modular array designs where all feeds and OMTs are fabricated in a platelet stack-up assembly;
- modular designs based on individual dual-polarization feed systems with OMTs, each cascaded with two independent LNA chains or with a single dual-polarization LNA chain;
- modular designs based on dual polarization feed system with cryogenic "active OMT" that integrates LNAs.

We adopt a miniaturized modular design that does not require re-imaging optics, where the array is placed at the Gregorian focus, in direct view of the sub-reflector. We also discuss solutions for different cryogenic arrays and set the constraints in terms of physical footprint size of each of the receiver modules.

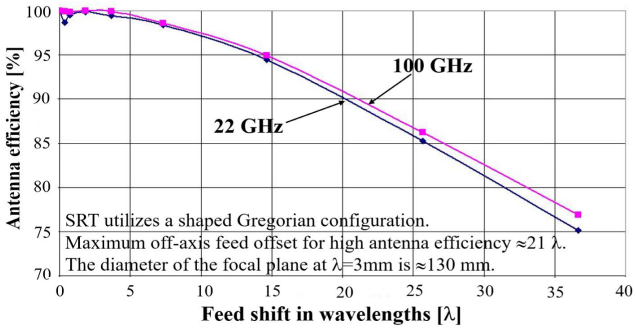

FIGURE 10. Simulated antenna efficiency at 22 GHz and at 100 GHz when the SRT is illuminated from the secondary (Gregorian) focus versus feed offset from the on-axis feed. The offset on the focal plane (orthogonal to the optical axis) are expressed in wavelengths ($\lambda = 3$ mm for $\nu = 100$ GHz). The antenna efficiency is normalized to the on-axis value, $100 \times \eta_{\text{eff}}(s)/\eta_{\text{eff}}(0)$, where $s = d/\lambda$ is the feed shift in wavelengths.

B. SIZE OF FOCAL PLANE AT THE SRT GREGORIAN FOCUS

The shaping of the SRT primary and secondary surfaces allows to minimize the spillover and the standing waves between the feeds and the subreflector. However, the shaped optics limits the telescope field of view achievable from the Gregorian focus. As the feed moves to off-axis positions on the focal plane the far-field pattern of the antenna becomes aberrated, with increased sidelobes and degradation in both cross-polarization level and antenna gain all of which contribute to a sensitive loss of antenna efficiency. The effects of the optical aberrations and the antenna beam pattern response depend on the antenna optics and on the beam pattern of the illuminating feed. We carried out electromagnetic simulations of the SRT radiation pattern and of the antenna efficiency by illuminating the telescope shaped optics with a corrugated feed-horn located at different offset positions relative to the Gregorian focus. Fig. 10 shows the results of such analysis for the SRT antenna efficiencies calculated at 22 GHz and at 100 GHz as a function of the linear shift d of the feed on the focal plane, expressed in wavelengths $s = d/\lambda$, normalized to the on-axis feed, i.e. 100 $\eta_{\text{eff}}(s)/\eta_{\text{eff}}(0)$. The purple curve, referring to the illuminating feed at 100 GHz, shows that to maintain high antenna efficiency (≈90% of the on-axis feed, equivalent to 0.5 dB loss in the antenna gain), the maximum offset of the feed must be less than ≈21 λ, corresponding to a maximum linear displacement on the focal plane of approximately ≈63 mm (at 100 GHz). We set the maximum loss of the efficiency that can be tolerated at any frequency across 70−116 GHz equal to ≈20% of the on-axis feed (equivalent to ≈80% of the on-axis efficiency, or 1 dB loss).

The requirement for the non-normalized antenna efficiency $\eta_{\text{eff}} \geq 0.5$ is achieved at all frequencies by confining the cluster of feed-horns within a radius of ≈65 mm from the telescope axis. The restrictions are imposed by the upper frequency edge, 116 GHz ($\lambda \approx 2.58$ mm), as the feed shift expressed in wavelength "s" is the highest ($65/2.58 \approx 25$). Therefore, the diameter of the SRT Gregorian focal plane for the $\eta_{\text{eff}} \geq 0.5$ efficiency requirement at ≈3 mm is ≈130 mm, which for a plate scale of ≈1.4 arcsec/mm corresponds to a FoV of ≈3 arcmin. There is no advantage in placing the array of feed-horns on a curved surface at the Gregorian focal "plane" because the SRT shaped optics has an almost planar image surface (a "planar Petzval surface") that does not need to be compensated by curvilinear arrangement of the apertures of the feeds to optimize the antenna efficiency. The feeds can be aligned on a planar surface, thus simplifying the array mechanics.

C. FEED SYSTEM

The radiating feeds of the W-band array must be designed to provide high-efficiency illumination of the SRT antenna at 12 deg half-angle ($f_2/D = 2.34$) across 70−116 GHz, with target edge taper value of ≈12 dB at 93 GHz (central frequency). The antenna efficiency specification $\eta_{\text{eff}} = \eta_t \eta_s \eta_p \geq 0.50$ must be satisfied for all feeds of the array, including those with the largest offset from the optical axis and must account for the coupling effects of the feed radiation pattern with the SRT shaped optics of primary and secondary mirrors. The detailed optical specifications include maximum acceptable levels of the feed-horn sidelobes (<−25 dB below the on-axis value of the co-polar component), cross polarization (<−25 dB), and return loss (>25 dB at feed-input), among others.

The RF requirements of the OMT across the 70−116 GHz frequency band are the following: input return loss >15 dB, insertion loss <0.7 dB (measured at room temperature), cross-polarization and isolation between outputs >25 dB. Our team has demonstrated experience in the design and characterization of mm-wave OMTs [52]–[56] and INAF in particular successfully developed prototypes of W-band OMTs and feed-horns, specifically for the ALMA (Atacama Large Millimeter Array) Band 2+3, 67-116 GHz, receiver cartridge [57], [58]. Such passive components are based on platelet design and have been successfully tested. We modified the INAF design of the ALMA Band 2+3 feed and OMT, re-optimized the feed for illumination of the SRT optics and the OMT for compactness. The feed-horn and OMT have a small footprint, suitable for integration in the W-band focal plane array. Such components have not been fabricated and tested yet. The mechanical drawings of the assembly are shown in Fig. 11, left panel, while a 3D sketch of the original feed and OMT cascade (previous to modification and adaptation to the SRT optics) is visible in the right panel. The feed aperture is ≈7×λ at the central frequency (Ø≈22 mm) and provides high-efficiency illumination of the SRT from the Gregorian focus across the 70-116 GHz frequency band.

The plots in Fig. 12 show the beam radius (the 1/e amplitude of the best-fit Gaussian beam) as a function of distance from the feed-horn aperture at 78 and 107 GHz. These values are used to estimate the clearance diameter of all apertures and optical elements in front of the feed-horns (IR filter, vacuum window, Solar filters, calibration load, pass through hole on the calibration wheel, etc…) and should be at least 4 beam

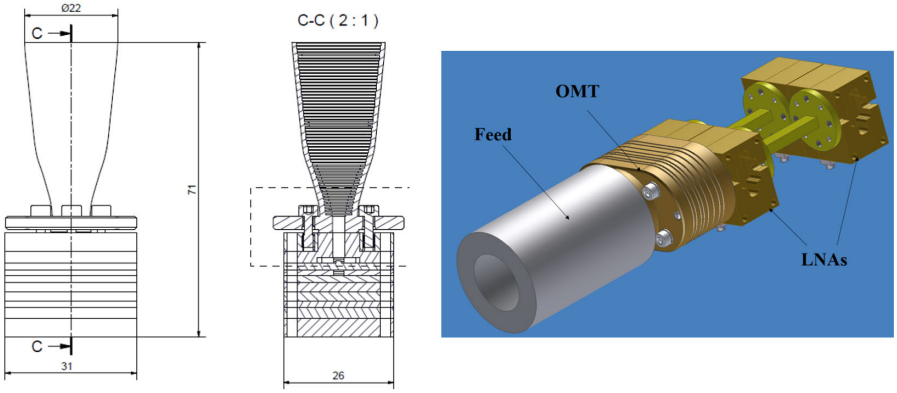

FIGURE 11. Left: Mechanical drawings of the platelet W-band feed-horn and OMT assembly with 31 mm footprint designed by INAF for illumination from the SRT Gregorian focus (70-116 GHz). Right: 3D sketch of W-band single-pixel dual-polarization cryogenic feed-system showing the feed-horn and OMT originally designed by INAF for ALMA Band 2+3 cascaded with two commercial cryogenic LNA modules (two LNAs per polarization channel, realizing a total gain G≈45 dB). The two LNA modules (each with gain G≈23 dB) are interconnected through a short section of waveguide with standard UG387 flange. An isolator could be used between each pair of LNAs to reduce the standing waves and improve the passband flatness.

radii at the lowest RF observing frequency, $\nu_{\rm RF} = 70$ GHz (where the beam is larger), to incur in negligible truncation loss. For example, at 100 mm distance from the feed horn aperture the beam radius at 78 GHz (not the lowest frequency of the bandwidth) is 24 mm, and the required minimum clearance aperture diameter is 96 mm (at that frequency).

We note that aperture-limited feed horns of the type illustrated in Fig. 11 have a typical diameter of order 3 w_0, where w_0 is the beam waist. Aperture-limited feed-horns have a beam waist that is essentially independent of wavelength, thus the beam size versus distance varies linearly with the wavelength in the far-field. If placed directly at the focal plane without re-imaging optics, these horns provide a non-optimal frequency-dependent edge taper illumination of the secondary and primary reflectors, resulting in a reduced antenna efficiency towards the band edges and optimum coupling only near the band center. This effect is due to under-illumination of the dish at the higher frequencies and over-illumination (high spill-over) at the lower frequencies of the band. However, non-optimum antenna coupling from the radiating feed can be tolerated within given limits, as long as the specification of $\eta_{\rm eff} \geq 0.5$ is fulfilled. INAF suggested the receiver architecture described in Section VII, which places the array directly at the Gregorian focus [59], with no re-imaging optics (see Appendix C for further discussion).

D. ARCHITECTURES OF INDIVIDUAL CRYOGENIC RECEIVER PIXEL ELEMENT

The individual array pixels comprise a feedhorn, an OMT and LNAs (typically two chained LNAs for each polarization channel are required in W-band), to be located inside the cryostat and thermalized at ≈15-20 K to minimize the system noise. A representative 3D image of an individual dual-polarization pixel that utilizes realistic component feature sizes is shown in the right panel of Fig. 11, where the

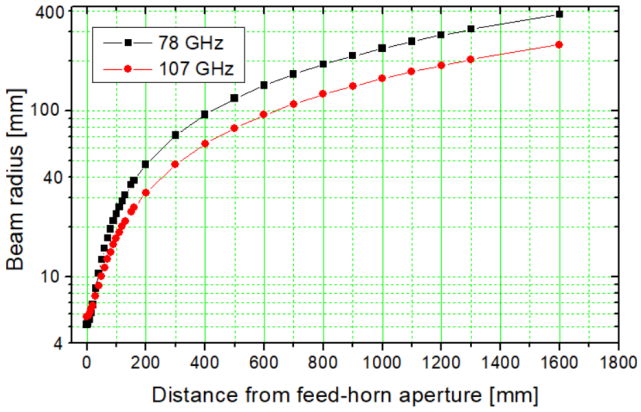

FIGURE 12. Simulated beam radius in mm (logarithmic scale) versus distance from aperture of the feed-horn designed by INAF for optimum illumination of the SRT. The beam waist radius is provided at 78 GHz and 107 GHz.

INAF designs of the ALMA Band 2+3 feed-horn and OMT prototypes are cascaded with two cryogenic LNA modules per polarization channel (four LNAs in total). There, the LNA modules are interconnected through a short section of WR10 waveguide with standard UG387 flange. The final architecture of the cryogenic receiving chain might adopt different configurations, as described in Appendix D.

E. CRYOGENIC LOW NOISE AMPLIFIER

The specifications of the cryogenic LNAs depend on the adopted receiver architecture. They shall be chosen to guarantee a SSB receiver noise performance, when measured in front of the receiver vacuum window, of less than 60 K over 80% of the RF band for all pixels/polarizations. The receiver noise budget estimate indicates that the noise performance at the input of the first LNA stage should be $T_{\rm N} < 35$ K (see Fig. 8). Here, we refer to the example of a receiver

architecture consisting of two LNA modules in cascade for each of the polarization channels, as depicted in the block diagram of Fig. 4. The first cryogenic LNA module shall deliver ultra-low noise performance, $T_N \approx 30$ K, and a gain of order 23 dB. LNA modules with the required performances are commercially available and are being further developed and improved for the ALMA Band 2+3 project [60]. The total gain of the two LNA stages shall be carefully chosen to satisfy at the same time noise and linearity requirements of the receiver: on one hand, a high gain would be desired to reduce the noise of the following stages (down-converter, IF switch, fiber optics link, etc.) to a negligible level; on the other hand, the receiver should have a linear response and operate well below the 1dB compression point. Therefore, the total gain of the cryogenic LNAs should be chosen to avoid the risk of saturation of the last LNA stage due to the large input bandwidths. For example, the input power expected at the first cryogenic LNA input, when observing a ≈300 K load, is of order −65 dBm (assuming an input bandwidth of ≈ 60 GHz). For a total gain of the two cascaded LNAs of ≈ 46 dB, an output power of −19 dBm would drive the last LNA stage near the non-linearity regime, for typical LNA output 1 dB compression point P1dB≈-10 dBm. For solar observations, the equivalent quiet Sun emissivity of ≈ 8000 K, would saturate the receiver.

Various solutions can be used to mitigate this problem, as described in Appendix E. For quiet Sun observations, we reduce the RF input bandwidth injected into the LNAs chain using a quasi-optical band pass filter at the receiver input, while for solar flare observations, where Sun emissivity of 10^5 K or greater could be expected, LNA bias de-tuning for receiver gain reduction will be studied.

The LNA module(s) must be designed to be compatible for integration with the other array elements (in terms of electrical/mechanical features, DC connector and placement, number of biasing wires, etc.) and comply with the cryogenic power requirements in terms of thermal power dissipation.

F. 4 × 4 ARRAY CONFIGURATION AND SRT RADIATED BEAMS

In order to accommodate a large number of W-band pixels on the usable "high-efficiency" focal plane area of the shaped Gregorian SRT telescope (with no re-imaging optics), i.e. within a maximum diameter ≈130 mm, it is necessary to adopt miniaturized components and utilize non-standard W-band waveguide flanges. The representation of a possible 4 × 4 array configuration with ≈31 mm feed spacing on the focal plane and the sketch of the associated SRT far-field beam patterns radiated in the sky are shown in Fig. 13. The separation of contiguous far-field beams is ≈43 arcsec. Fig. 14 shows the result of the electromagnetic simulations for the SRT radiated far-field beams, illuminated by the feed-horn of Fig. 9 (left panel). The radiation performance was simulated at 93 GHz using the GRASP commercial software (from Ticra, https://www.ticra.com/software/grasp/). In the simulations, we adopted a simplified antenna geometry with

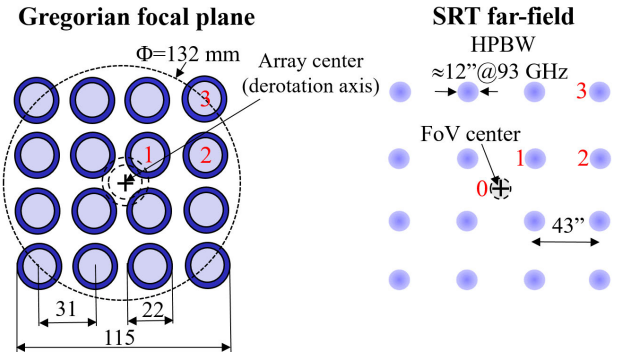

FIGURE 13. Example of configuration of the array with 4 × 4 feeds on the Gregorian focal plane (left panel) and corresponding beams projected in the sky (right panel). The axes of all feeds are enclosed in the "high antenna efficiency circle" with diameter Φ̂ =132 mm. The pixel labeled as 0 refers to a hypothetical feed located at the array center. Pixels labeled as 1, 2 and 3 corresponds to various offset positions.

an ideal primary and secondary reflectors with shaped profiles and no quadrupod legs. The 2D-color plots in the central column of Fig. 14 refer to the computed co-polar radiation patterns (fed from the horn vertical polarization channel), while those on the right column refer to the associated cross-polar radiation patterns. The top-panel 2D-color plots provide the expected beam patterns from a hypothetical central pixel, associated with the FoV's center, and are used as a reference for the performance of all 4 × 4 offset feeds. The 2D-color plots on the second, third and fourth panels of Fig. 14 show the SRT radiation patterns from the three different feed offset positions "1", "2", and "3". Calculated copolar antenna gain and efficiency values at 93 GHz at different position offsets are given in Tab. 6. The antenna gain and the antenna efficiency decrease by 0.5 dB and 8.2%, respectively, from center to corner pixel. For a hypothetical center-feed illumination, the SRT radiated beam would have rotational symmetry down to a level of −25 dB, while for the SRT offset-feed illuminations the radiated beam gets distorted. The four graphs of Fig. 15 show the 1D-cut of the antenna gains associated to feed offsets "0", "1", "2", and "3", for elevation angles θ in the range 0-150 arcsec from the boresight direction of the reference central feed illumination (FOV center).

The graphs of Fig. 15 associated with offset "1", "2", and "3" show that the beams have a good symmetry down to a level of approximately −10 dB below the peak, and are distorted below that level. The beam distortion, sidelobe, and cross-polarization levels are greatest for the most offset feed at position "3" (corner feed). The pointing (boresight) directions associated with the feeds at offset positions "1", "2", and "3" are found at angles of $\Delta\theta \approx 30.2$ arcsec, ≈67.5 arcsec and ≈90.6 arcsec, respectively, from the reference FOV center, in agreement with $\Delta\theta = \Delta x/D\,(f_2/D)^{-1}$. Here, $D = 64.002$ m, $f_2/D = 2.342$ (see Tab. 1), and $\Delta x =$ 21.92 mm, 49.015 mm and 65.76 mm, for distances from the array center to feed centers at positions "1", "2", and "3", respectively. The insets inside each of the graphs of Fig. 15 also highlight the offset feed positions (four "1",

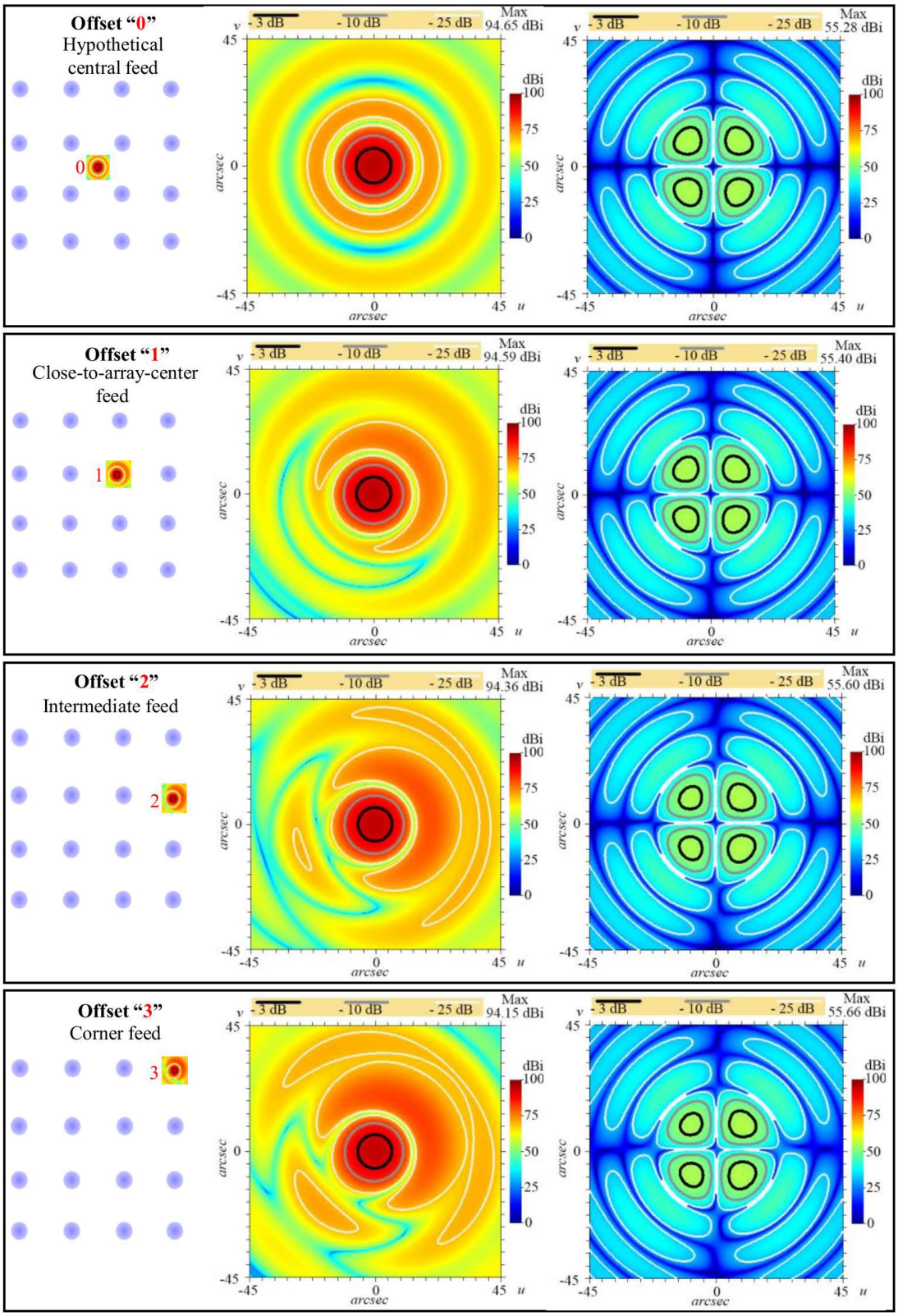

FIGURE 14. GRASP simulations at 93 GHz of the radiated far-field beam patterns of the SRT telescope illuminated by the corrugated feed of Fig. 9 (left panel). The feed is offset at the four different positions of the focal plane ("0", "1", "2", and "3"), as shown on the left column (see also Fig. 13). The images in the central column show the co-polar patterns, those on the right column the cross-polar patterns. The 2D-color plots illustrate the antenna gains, whose maximum values, in the 45 × 45 arcsec^2 field, are shown on the top right margin of each of the images. The antenna gain is color-coded on the vertical scale next to each graph (0-100 dBi range). The solid lines in black, grey, and white inside each 2D plot show, respectively, the −3 dB, −10 dB, and −25 dB levels below the maximum gain value. All field maps are centered on each relative co-polar maximum and the offset angles refer to the local reference system.

eight "2" and four "3") associated to the plotted beam, since, for symmetry reasons, they provide equivalent performance.

TABLE 6. Simulated SRT antenna gain and efficiency at rf band central frequency versus feed offset position on the focal plane.

Feed position	SRT antenna gain at 93 GHz[dBi]	Ant. efficiency η_{eff}(93 GHz)
0 (central)	94.65	0.751
1 (close-to-array-center)	94.59	0.7407
2 (intermediate)	94.36	0.7025
3 (corner)	94.15	0.6693

Fig. 16 shows possible scanning geometries for the 4 × 4 configuration that could be used for mapping large angular areas on the sky at three frequencies: 70 GHz, 93 GHz and 116 GHz. An almost Nyquist-sampling is achieved at all frequencies with two sub-scans. The profiles shown on the left of each panel represent the overlapping level of all the combined beams.

Adoption of a feed spacing of ≈31 mm requires single-pixel receiver modules with a maximum cross-section of ≈31 × 31 mm^2. Our design of the feed-OMT cascade with such footprint (left panel of Fig. 9) can be used to form a 4 × 4 array. However, a footprint reduction of the LNA and of the isolators (if used), is also required. In the following sections, we present two innovative single-pixel receiver design options that would be suitable for the required 4 × 4 array integration, one based on miniaturized dual-polarization LNAs, the other based on "active OMTs".

G. 4 × 4 ARRAY BASED ON MINIATURIZED LNAS MODULE

Fig. 17 shows a 3D sketch of a 4 × 4 cryogenic array with ≈31 mm pixel spacing. The architecture is based on 16 identical cascades of the following receiver chain elements: feed, OMT, and dual-channel W-band LNA module. We refer to the latter as a "dual-polarization LNA module", because each of the two LNA "channels" amplifies the linearly-polarized signal at the OMT output. Such an innovative module would require significant engineering development and should be customized for this specific application. The main development challenges would be in the packaging of the various components. The dual-pol LNA module should feature two waveguides at its inputs (and two waveguides at its outputs), one per polarization channel, and deliver low noise performance across 70−116 GHz (in the range T_{N} ≈25-40 K) for both polarization channels, with approximately ≈45 dB gain, good matching at all ports, and very high isolation between independent inputs and outputs. The dual-polarization LNA module would adopt non-standard UG387 waveguide flanges and DC bias connectors placed on the module output side. It would incorporate four MMIC LNAs, two in cascade for each of the polarization channels (each MMIC amplifier would deliver a ≈23 dB gain). We discussed our miniaturized dual-channel LNA concept with a company that has demonstrated experience in the development of W-band LNAs. Although the design details of our dual-polarization LNA module have not been worked out, we were confirmed the feasibility of our conceptual design

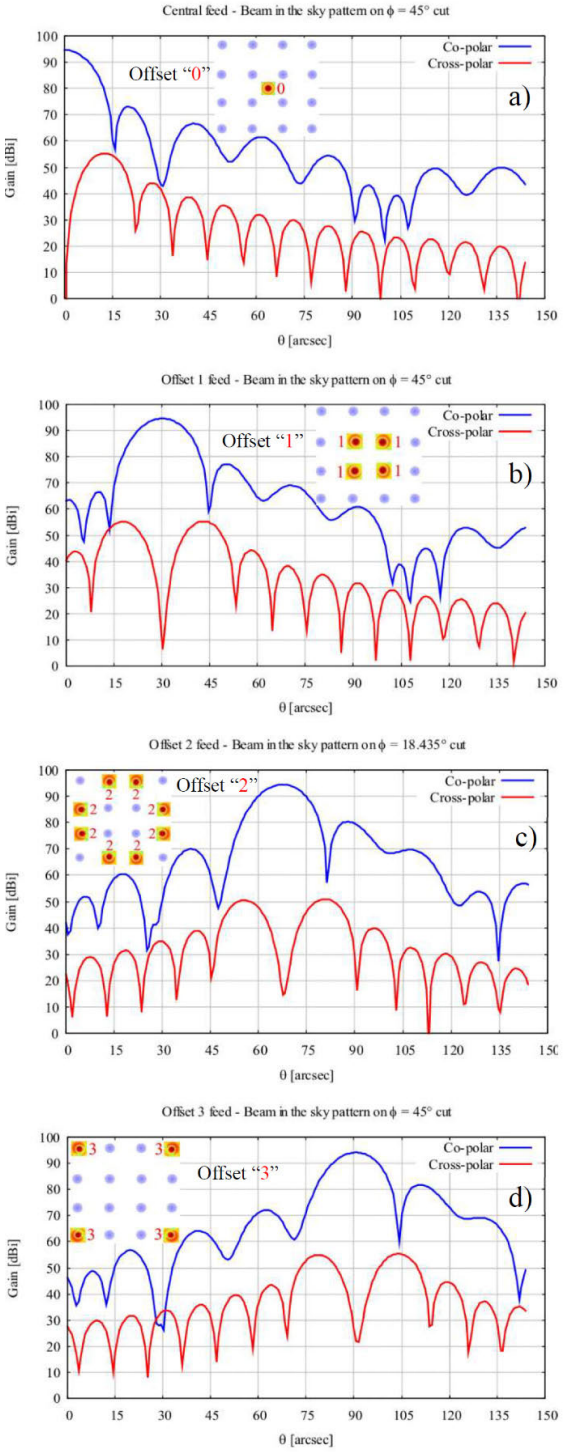

FIGURE 15. Simulated pattern cuts of SRT antenna gain illuminated by feeds at offset positions "0" (on-axis antenna reference, top panel, "a"), "1" (second panel, "b"), "2" (third panel, "c") and "3" (bottom, "d"). The co-polar and cross-polar antenna gains, expressed in dBi, are shown in blue and red lines, respectively. The gain patterns are referenced to the main optical axis of SRT. They refer to angles ϕ_k = 45°+k 90°, with k = 0, 1, 2, 3 for the four beams of offsets "1" and "3", and to ϕ_{k+} = 18.435°+k 90° and ϕ_{k-} = 71.565°-k 90° with k = 0, 1, 2, 3 for the eight beams of offset "2".

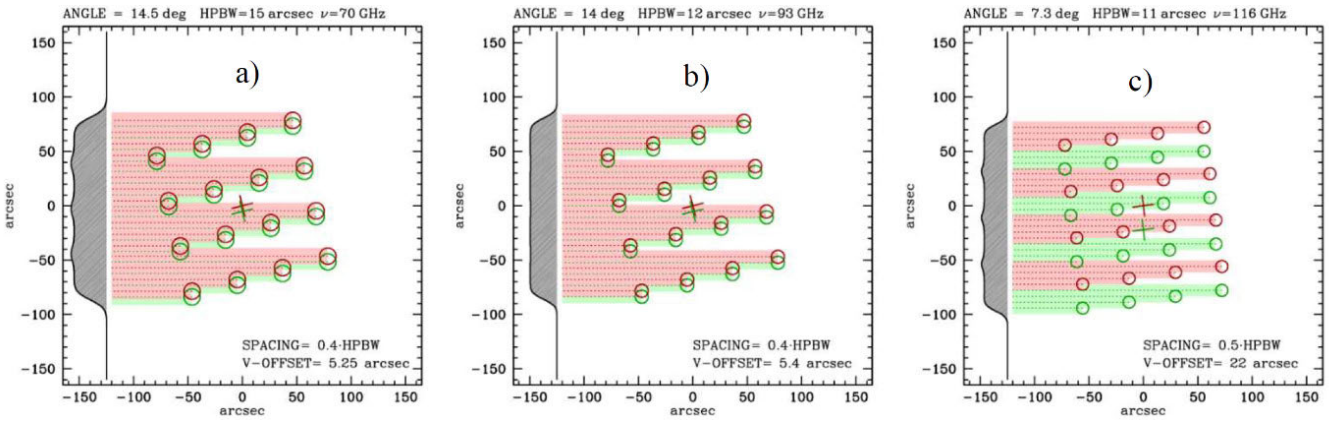

FIGURE 16. Scanning geometry with the 4x4 array for mapping with respect to the scanning direction at 70 GHz (left panel, "a"), 93 GHz (center panel, "b") and 116 GHz (right panel, "c"). Near-Nyquist sampling is achieved with two sub-scans. The overlapping of the beams is shown on the left of each panel as a shaded area.

of the module, as all of its parts (MMICs, waveguide circuitry, waveguide flanges, DC connectors, bias circuits) can be incorporated in a mechanical module with a 31×31 mm^2 footprint area.

H. 4 × 4 ARRAY BASED ON "ACTIVE OMTS"

An alternative to the OMT and miniaturized LNAs is based on an ''active OMT'' module. Such a device consists of a dual-polarization receiver module based on an OMT that integrates MMIC low-noise amplification stages. The design would be similar to the one presented in [47] and [61]. 3D sketches of the W-band single-pixel module based on an active OMT is illustrated in Fig. 18, where the model shown in the left panel has been fabricated and successfully tested. The arrangement of the 4×4 array with active OMT is similar to that with dual-polarization LNA, shown in Fig. 17.

VII. LAYOUT OF W-BAND MULTIBEAM RECEIVER

The design concept of the W-band multibeam receiver, associated with the block diagram of Fig. 4, is shown in Figs.19-20. The images illustrate a possible overall mechanical structure of the instrument and the interfaces between its sub-systems. The design fulfills the specifications and requirements listed in Sect. III. The main sub-assemblies of the receiver are listed in Tab. 7.

The maximum dimension of the full receiver along the optical axis is 2450 mm. The phase centers of the feedhorns must be positioned with precision along the optical axis with respect to a plane located on the mechanical support frame. The phase centre of the designed feed is close to the feed aperture at all frequencies across 70-116 GHz. The axis of the receiver mechanical derotation shall be aligned with the optical axis of the antenna and with the geometrical centre of the array shown in Fig. 13. Fig. 21 shows images of the receiver mounted on the Gregorian turret through its mechanical support. This preliminary receiver design concept has considered aspects related to ease of service and repair. The detailed design approach shall consider component access,

TABLE 7. Main receiver sub-assemblies.

#	Sub-assembly item
1	W-band cryogenic focal plane array, with feeds, OMTs, and LNAs
2	Cryostat with CTI cryogenerator and vacuum components, including vacuum window and IR filter
3	Multi-pixel sideband separating down-converter
4	Local Oscillator (LO) system
5	Solar filters/attenuator and calibration load switching system in front of the receiver vacuum window
6	Cabinet with electronics racks, including the Monitor and Control Unit and the IF selector
7	Mechanical derotator
8	Cable wrap with IF coaxial cables, helium lines, and receiver output interface
9	Mechanical support frame for bolting the receiver to the Gregorian Receiver Positioner

particularly with respect to the multi-pixel receiver (LNAs, mixers, etc…) in case of their failure. In particular, the final design shall allow a procedure for easily accessing and replacing the components, keeping in mind cable connections, wires and cables routing, component interconnections, and interfaces. The cryostat design shall allow simple maintenance of the cryocooler, which must be removed from the cryostat without dismounting the receiver from the Gregorian focus. This requires that enough free space is left below the cryocooler to allow its extraction and replacement during maintenance, as in the proposed design concept.

VIII. CRYOSTAT, CRYOGENERATOR, AND MECHANICAL PARTS

In this section, we describe the feasibility study of the cryostat and of its parts, including the cryogenerator, the vacuum window, IR filter and other components internal to the vacuum container that will host the cryogenic array receiver modules. Furthermore, we discuss the mechanical derotator and the calibrator insertion mechanism.

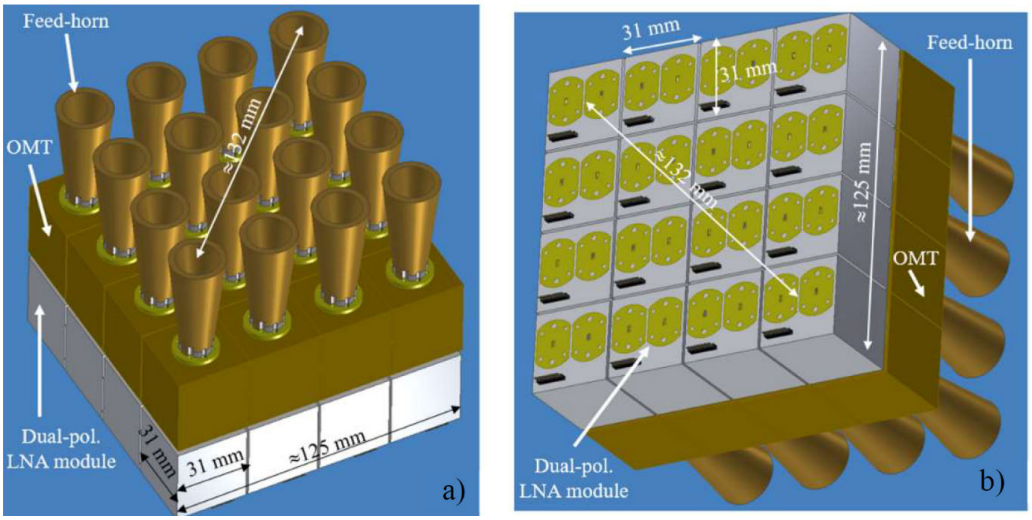

FIGURE 17. Sketch of W-band 4x4 cryogenic array, where each single-pixel receiver chain is based on a cascade of a feed-horn, OMT and "dual-polarization LNA" cryogenic module. The OMT waveguide outputs and the waveguides inputs and outputs of the dual-polarization LNA module utilize non-standard waveguide flanges (for example an UG387 flange with only two screws and with "cuts" that makes them fit into 15 mm spacing on the waveguide E-plane). Views from the feed horns side (left panel, "a") and from the dual-polarization LNA modules side (right panel, "b").

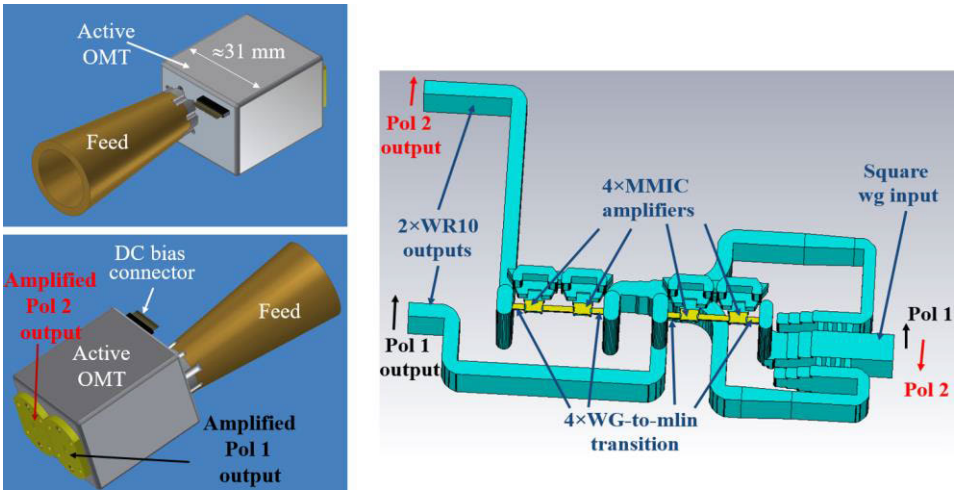

FIGURE 18. Top left and bottom left: 3D sketch of W-band single-pixel dual-polarization module based on feed and "active OMT". Right: Illustration of the inner structure of the "active" OMT based on a waveguide reverse-coupler OMT (from [47], [54] and [61]). The module design features the square waveguide input, supporting the propagation of two orthogonal polarization states associated to Pol 1 and Pol 2, and the amplified single-mode WR10 waveguide outputs for Pol 1 and Pol 2, each of which is extracted from a different waveguide. The passive part of the waveguide circuitry includes a reverse-coupler OMT, whose output waveguides are cascaded to MMIC LNAs to which the signal is couple through waveguide probes.

A. CRYOGENERATOR AND HELIUM GAS LINES

The design of the cryogenic components and the cryostat assembly (choice of LNAs, number of LNA bias wires, infrared filter, etc.) shall minimize the thermal power loading to allow proper cooling of the parts by a single closed-cycle helium refrigeration cryogenerator (cryocooler). The cryocooler will be bolted to the receiver vacuum container at the Gregorian Receiver Positioner. It is connected to its driving compressor, which is located in the antenna Alidade Equipment Room (on the lower part of the SRT antenna), through ≈96 m long helium gas supply and return lines. The W-band receiver will comprise ≈4 m long 0.5-inch diameter self-sealing flexible interconnecting helium gas lines, to be located in the cable wrap along with the IF coaxial cables. The cryocooler, based on the Gifford-McMahon thermodynamic cycle, must be compatible with the commercial compressor (model CTI 9600) and helium lines that will be available at the SRT. The cryocooler shall be either a Cryodyne model CTI 350CP or CTI 1020 from Helix Technology Corporation (at present part of Brooks Automation Inc.) and operate

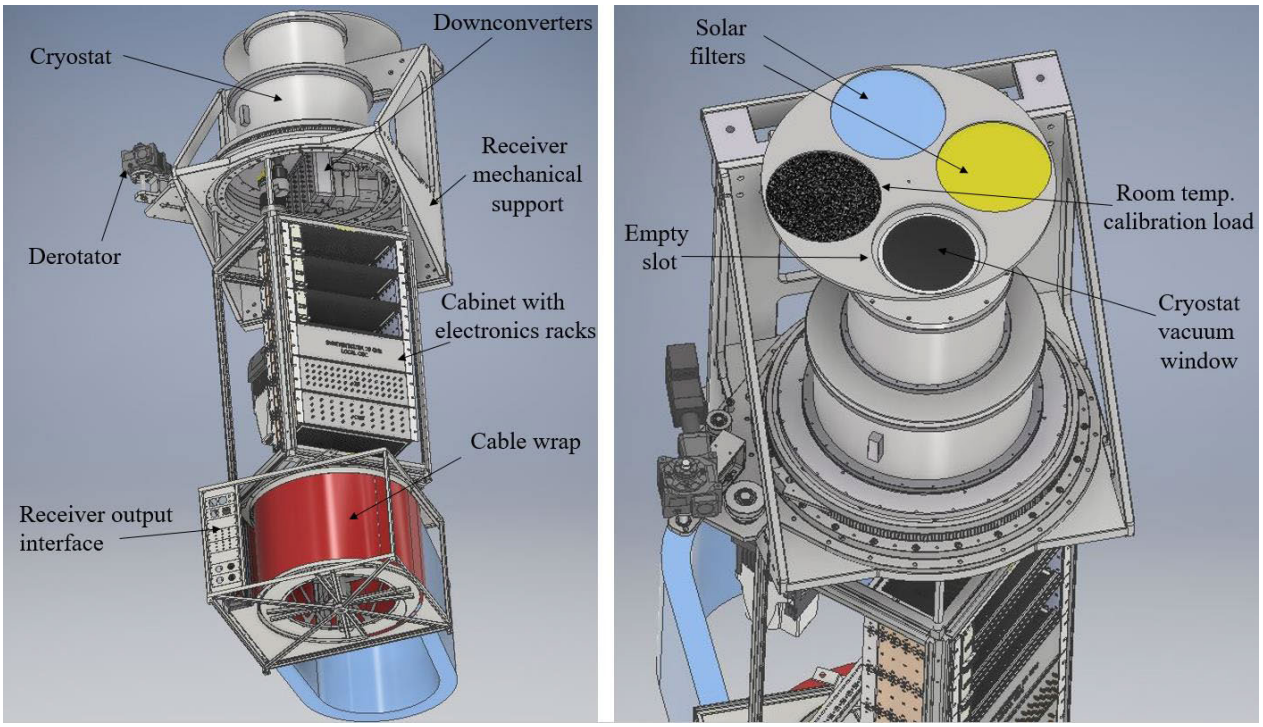

FIGURE 19. 3D sketch of the W-band multibeam receiver. View of the full instrument showing the cryostat with down-converter, mechanical derotator, cabinet with electronics rack and mechanical frame for mounting on the Gregorian receiver positioner (left). Rotating wheel for selection of Solar filters, calibration load or empty slot (right panel). The view shows the selection of the empty slot with the receiver looking at the cold sky.

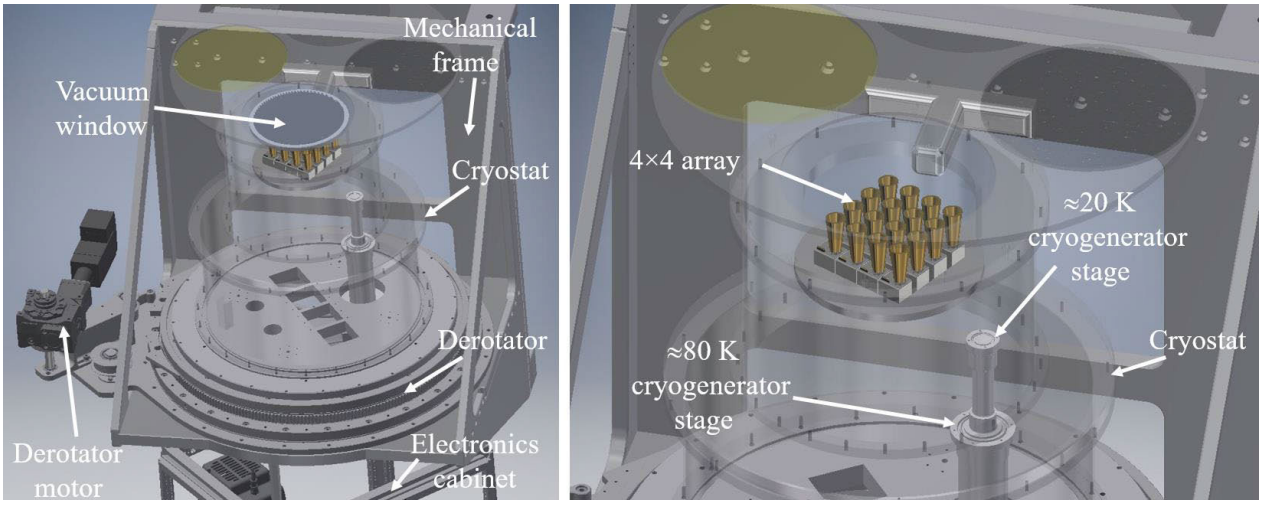

FIGURE 20. 3D sketch of the inner part of the cryostat showing the 4 × 4 cryogenic array and the CTI cryogenerator (cold finger). Left panel: the vacuum window is located in front of the feed-horn cluster. Right panel: view of the 4 × 4 array.

at 50 Hz. Both models adopt two cryogenic stages. Model CTI 350CP provides a heat lift capacity of 4 W at 20 K and 20 W at 77 K simultaneously, while model CTI 1020, designed for higher capacity application, provides 12 W of heat lift at 20 K and 35 W at 77 K simultaneously.

B. CRYOSTAT DESIGN AND VACUUM PUMPS

The cryostat allows to accommodate the array pixels, provides the necessary rigidity and heat-lift capacity, and allows access to all interfaces related to installation and operation at the SRT. The design concept is based on two concentric cylindrical structures, where the smaller diameter structure with $\phi \approx 300$ mm hosts the vacuum window, the IR filter, and the cryogenic array, while the larger diameter structure with $\phi \approx 630$ mm hosts the cryocooler, the low-thermal conductivity WR10 waveguides connecting the outputs of the cryogenic LNAs to the cryostat backplate and the internal thermal connections that guarantee temperature uniformity

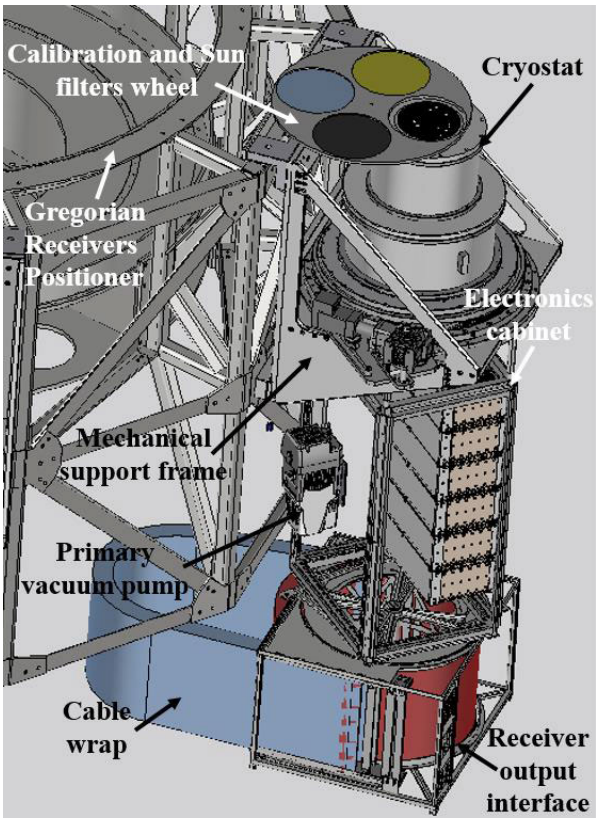

FIGURE 21. 3D sketch of the W-band multibeam receiver mounted on the Gregorian rotating turret through it mechanical support frame. Perspective view showing the Solar filters/attenuator and calibration load switching system in front of the receiver vacuum window.

on the inner stages. This design allows to minimize the cryostat internal volume and the heat load on the inner stages compared to a design with a single cylindrical structure and diameter $\phi \approx 630$ mm. The heat break between each thermal stage is provided by low thermal conductivity G10 epoxy cylindrical bars distributed between the main inner supports on the ≈20 K and ≈80 K stages. An IR radiation screen and insulation layers are adopted to minimize the heat load. A heat-load analysis of the cryostat cryogenic stages allows evaluating the thermal load on the two cryocooler cryogenic stages due to the main cryostat parts, which include the vacuum window, the IR filter, the IR radiation from the cryostat, and shields based on their surface treatment, the superinsulation, the power consumption of all the active components, the thermal links, the DC wiring, thermal breaks, etc…

The outer part of the larger cylindrical structure of the cryostat is designed to incorporate a mechanical interface for connection to the mechanical derotator. Both the cryostat (with focal plane array inside it) and the cabinet with electronics rack will be rotated by the mechanical derotator during the observations.

The cryostat concept illustrated in Figs. 19-21 requires detailed mechanical analysis, including mechanical stress, flexure, resonance frequencies and thermal distribution. The cryogenic array components will be thermally linked to the second stage of the cryocooler and will operate at a physical temperature of ≈ 20 K. The cryostat design must take into account the heat load present on the cryogenic system thermal stages resulting from the various parts. The thermalization of the cryogenic components must ensure that uniform temperature distribution is achieved for all receiver pixel elements, which must deliver similar radiometric performances.

The receiver will include a monitoring of the temperatures of the two cryostat cryogenic stages (≈20 K and ≈80 K) by four temperature sensors (for example Silicon diode sensors from Lake Shore Cryotronics model DT-670B-CU): two sensors placed in thermal contact with the cryocooler cold fingers at ≈20 K and ≈80 K (one for each stage), one sensor placed on one of the LNAs of the cryogenic array (at ≈20 K) and one placed on the IR shielding at ≈80 K.

Vacuum pumps (primary and turbo molecular secondary pump) and a vacuum gauge will be permanently installed and connected to the receiver cryostat while in operation on the SRT telescope. An electromagnetic vacuum valve will be installed between the cryostat and the turbo molecular pump to guarantee the necessary low vacuum pressure in the vacuum chamber while the turbo molecular pump is off and the vacuum valve is closed. The turbo molecular pump and CTI cold head will be controlled remotely by a monitor and control (M&C) unit.

C. VACUUM WINDOW AND INFRARED FILTER

The material, diameter and thickness of the cryostat vacuum window shall be chosen to support the atmospheric pressure (with sufficiently high security factor) and reduce its bending to a negligible level to avoid phase distortions of the propagated beams. The window diameter must guarantee negligible truncation loss for all receiver beams and be dimensioned with at least 4 beam radii at the lowest observing frequency by considering that the array must be confined within a ≈130 mm diameter. If located close to the feed apertures, where the beams are narrow, the vacuum window could have a 200 mm clear aperture (see Fig. 22) and, if made of HDPE (High-Density Polyethylene), with ≈12 mm thickness (corrugations excluded). The IR filter could consist of PTFE (Poly Tetra Fluor Ethylene) with 200 mm clear aperture and ≈6 mm thickness (corrugation excluded). The refractive index $n = (\varepsilon_R)^{0.5}$ and loss tangent tanδ for HDPE are respectively, $n = 1.53$ and $\tan\delta = 3 \times 10^{-4}$ at $\nu \approx 100$ GHz at ambient temperature. The absorption loss per unit length for HDPE is $\alpha \approx 0.06$ dB/cm. In general, the loss per unit length is proportional to frequency ν and given by $\alpha = (2\pi\nu n tan\delta)/c$ (c is the light speed in vacuum). Therefore, the thickness of the vacuum window should be minimized to reduce its insertion loss, as this increases linearly with thickness and strongly impact the receiver noise temperature because it is placed at room temperature. Triangular corrugations machined on each side of the window/filter would provide wideband anti-reflection coatings (Fig. 22).

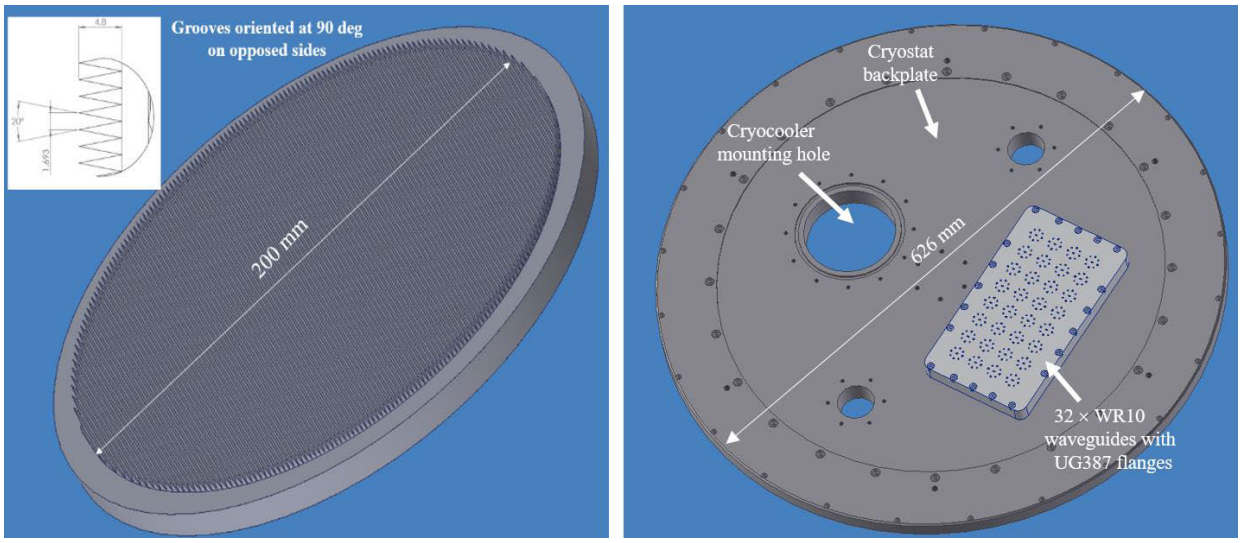

FIGURE 22. Left: Sketch of wideband vacuum window or IR filter with 200 mm clear aperture for 70-116 GHz. The corrugations have triangular shape with 20 deg angle and 4.8 mm depth Right: 3D sketch of cryostat backplate showing the mounting hole of the cryocooler and the vacuum-sealed plate with 32 WR10 waveguides and standard UG387 flanges that outputs the amplified signals from the cryogenic LNAs (transported through low thermal conductivity waveguides from the 20 K stage to the 293 K stage of the cryostat backplate).

D. MECHANICAL DEROTATOR AND RECEIVER OUTPUT INTERFACE

The rotation of the imaged field during source tracking occurs with any telescope utilizing an alt-azimuth mount, like the SRT. The azimuth axis rotates around a vertical line passing from the center of the telescope to the zenith, while the elevation axis rotates about a horizontal axis. Both axes must rotate at different rates to maintain the object in the field of view fixed relatively to the array pixels during tracking. As the Earth rotates about its axis, the central object in the field of view will remain centered but other objects in the FOV will appear to rotate with elapsed time. To compensate this effect, the W-band receiver incorporates a mechanical derotator to avoid field derotation and maintain the parallactic angle. The derotator is actuated by a motor and controlled remotely, as the rotation depends on the azimuth and elevation of the object being observed. The rotation rate required to compensate for Earth rotation during source tracking is infinite at the Zenith as it scales as 1/cos(Elev), where the elevation angle ''Elev'' is 90^0. Therefore, it is not possible to observe sources during their transit near or at the Zenith. The maximum derotation rate of the W-band multibeam will allow observation of objects up to a maximum elevation of 85^0. The cryostat and the four four-pixel down-converter connected to it will be derotated along with the hardware that will be located in the electronics cabinet shown in Figs. 19-21. The derotator will attach to the external part of the cryostat. However, the IF cable wrap located below the electronics cabinet will be integral with the Gregorian Receiver Positioner. The cable wrap will incorporate 32 (plus spares) ≈4 m long coaxial cables for IF transportation from the internal IF switch matrix to the receiver output interface located at the cable wrap panel. Helium return and supply lines and power lines from/to the cryocooler, a coaxial cable with the 10 MHz reference from the Hydrogen maser, optical fibers for communication and M&C as well as spare signals from the spare 13.66-17.33 GHz LO synthesizer will also go through the cable wrap and be available at the cable wrap panel, which defines the output interface of the receiver (see Figs. 5, 19 and 21).

E. SOLAR FILTERS-ATTENUATOR AND CALIBRATION MECHANISM

Two solar quasi-optical band-pass filters (BPFs), with central frequencies at 78 GHz and 110 GHz, each with relative RF band of order 6%, could be adopted to reduce the signal power and mitigate the receiver saturation problem. The solar filters can be positioned in the signal path by a suitably designed switching mechanism, mounted in front of the vacuum window shown in Figs. 19 and 21. The switching mechanism includes a calibration system with one room-temperature calibration load, i.e. an absorbing material at ≈293 K (for example Eccosorb from Emerson&Cuming Inc.) that absorbs the RF power and minimizes reflections, reproducing a ''black body''. The calibrator has an embedded temperature sensor that provides a temperature reference scale for all dual-polarization feeds of the array. The solar filter and calibration wheel will be remotely controlled by a motor. The wheel can be fixed either on the cryostat or on the external mechanical support. In the latter case, the filters and calibrator would rotate with respect to the feed-horn array during source tracking (while the cryostat is rotated by the mechanical derotator). The wheel mechanism has four positions: 1) blank pass through; 2) solar filter centered at 78 GHz; 3) solar filter centered at 110 GHz; 4) ≈300 K calibrator. Magnetic Reed sensors or encoders interlock can be used to read the wheel position.

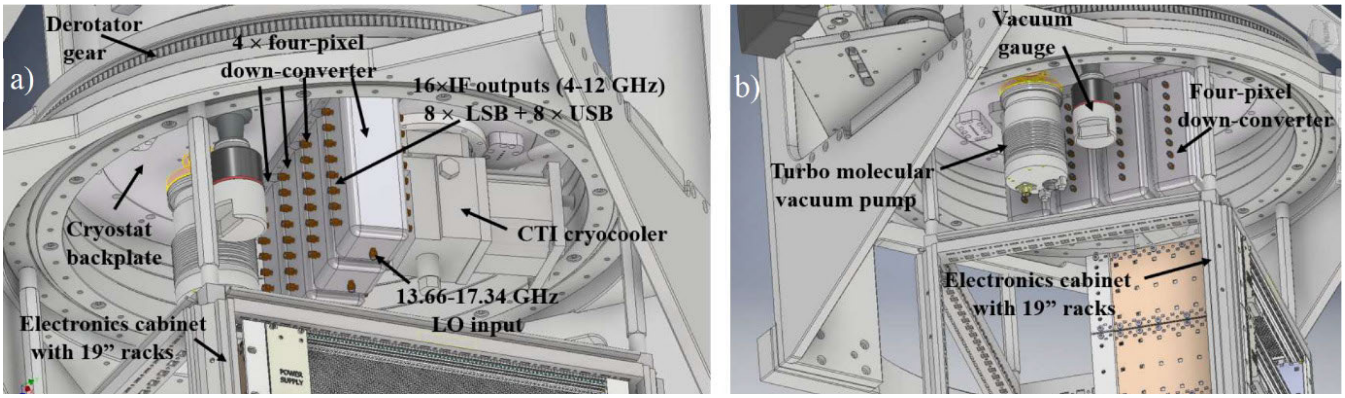

FIGURE 23. 3D sketches (left "a", and right, "b") showing the four independent four-pixel down-converter modules attached to the cryostat backplate. The backplate hosts the vacuum valve (not shown), the turbomolecular vacuum pump, the vacuum gauge, the CTI cryogenerator, the WR10 waveguide vacuum feedthroughs and the vacuum feedthrough DC connectors for biasing the internal components of the cryostat.

IX. DOWN-CONVERTER

As discussed in Section III, the W-band multibeam heterodyne receiver can adopt different architectures in terms of pixel number, type of LNAs, down-conversion scheme, instantaneous band processed by the backend, etc.. In this feasibility study, we refer to the 4×4 array with sideband separating heterodyne down-converter modules located outside the cryostat, as depicted in the block diagram of the receiver of Fig. 4. The signals available from the 16 cryogenic dual-polarization feed-systems are transported by $4 \times 4 \times 2 = 32$ waveguides to the room-temperature cryostat backplate and connected to WR10 waveguide vacuum feedthroughs with UG387 flanges shown on the right panel of Fig. 22. Vacuum sealing through the signal paths of the waveguide can consist of low-loss low-input reflection broadband waveguide vacuum window with low leak rate ($< 10^{-8}$ mbar l/sec) based on a thin Mylar sheet ($\approx 25\ \mu$m) clamped between waveguide flanges with an O-ring seal, or on alternative broader band hermetic designs with low leak rates. Waveguide band pass filters (BPF) for the 70-116 GHz band, located outside the cryostat, are attached to the cryostat backplate in front of four four-pixel down-converter modules shown in Fig. 23. Each of these four-pixel modules is based on eight sideband separating (2SB) mixers that utilize GaAs semiconductor Schottky technology. Each down-converter module has 8 WR10 waveguide inputs and $16 \times 4 - 12$ GHz IF outputs. It receives the signals from a row of 1×4 dual polarization cryogenic pixels and down-converts them to $16 \times 4 - 12$ GHz IF outputs, 8 LSB and 8 USB. In total, the four down-converters deliver 64 coaxial output signals across the 4−12 GHz IF band, 32 USB and 32 LSB. The four-pixel down-converter modules can be designed to incorporate WR10 waveguide band pass filters at its input to select the 70−116 GHz band from the cryogenic amplifiers. The design concept of the "active" sideband separating down-converter modules is similar to the one developed for the AETHRA W-band multibeam receiver [47] where fully integrated MMICs [62], [63] have been used. However, here we propose to use fundamental in-phase and quadrature I/Q W-band mixers, rather than sub-harmonic mixers, and the adoption of four-pixel modules rather than three-pixel modules. The outputs of the I/Q mixer are amplified by IF amplifiers prior recombination by a 90 deg IF hybrid. The main electrical specifications of the active down-converter module are 0 dB gain and 8000 K noise (at room temperature) when accounting for a $\approx$10 dB mixer conversion loss and 10 dB amplification by the cascaded IF LNAs. Bandpass filters covering the 4−12 GHz band are used at the module IF outputs. The image sideband rejection performance depends on the amplitude and phase balance at the RF and IF hybrids [64], [65], as well as on the passband flatness in front of the mixer itself, which includes the gain flatness of the cryogenic W-band LNAs. A detailed design of the RF and IF circuits is needed to achieve the 10 dB sideband rejection specification for all pixels.

One four-pixel down-converter consists of three parts and contains eight RF-input WR10 waveguide with standard or custom-flanges, an eight-way LO splitter for 13.66-17.33 GHz baseband-LO distribution to eight internal down-converter MMICs, eight 4-12 GHz IF hybrids for the LSB/USB IF-outputs, and DC-bias circuitry. A block diagram of the fundamental frequency down-converter MMIC with integrated sextupler and medium power amplifier is shown in Fig. 4. The mechanical assembly and connection to the cryostat backplate of the four four-pixel down-converter is shown in Fig. 23. A four-way LO splitter (see the block diagram of Fig. 4) will split and distribute the baseband LO signal from the commercial LO synthesizer, located in the electronics rack, to the four four-pixel down-converters.

X. MONITOR AND CONTROL UNIT

The vacuum valve, the turbo molecular pump, the primary pump and the CTI cryocooler will be remotely controlled and monitored. For maintenance purposes, the cryostat vacuum pressure shall be permanently and remotely monitored by the vacuum gauge. In addition, monitoring of the cryogenic temperatures and monitoring and control of the cryogenic LNA bias is required. The array is monitored and controlled through the M&C unit, whose 3D sketch is shown in Fig. 24.

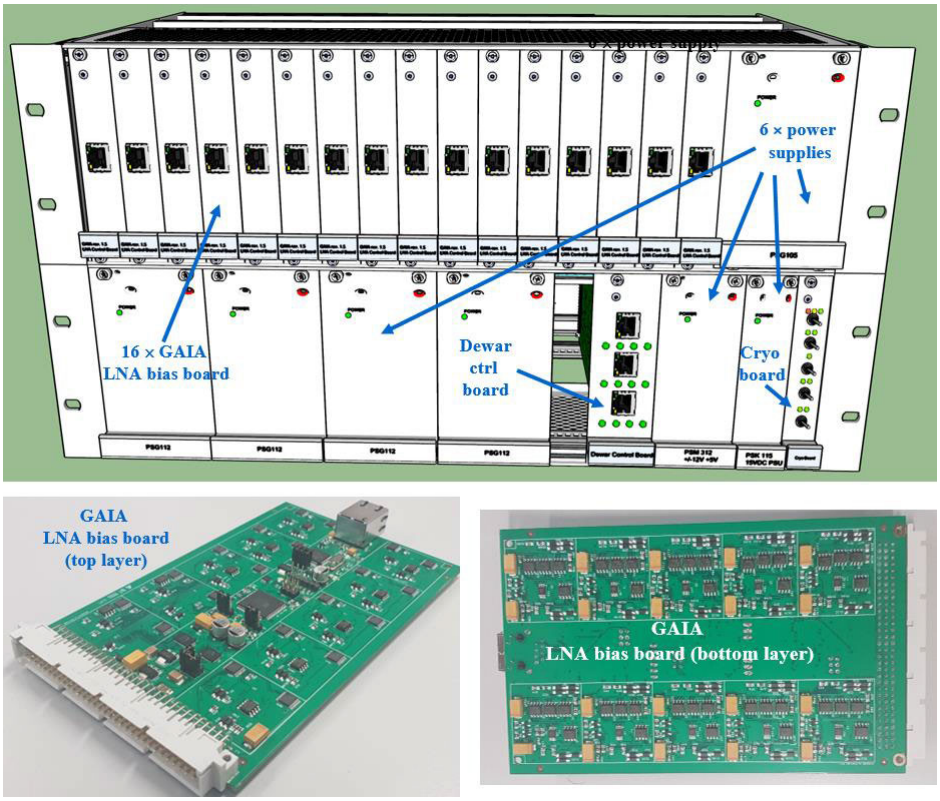

FIGURE 24. Top: 3D sketch of the monitor and control (M&C) unit of the W-band receiver. The 19" 6U rack includes 16 GAIA bias boards for the cryogenic millimeter-wave LNAs, the Dewar control board, the "cryo" board and six commercial power supplies. Bottom: Pictures of the GAIA LNA bias board developed by INAF (top layer on the left panel, bottom layer on the right panel).

The rack incorporates different types of electronic bias boards developed by INAF: the ''GAIA'' LNA bias board, the Dewar control board and the ''cryo'' board.

The GAIA board [66], [67] provides ultra-stable biasing of the W-band cryogenic LNA modules. GAIA is a 3U (1 rack unit being 44.45 mm) four-layer rack-mountable programmable digital bias board based on a microcontroller and on digital potentiometers designed for biasing, remote monitor and control of the gate voltages V_g and of the drain voltages V_d of cryogenic LNAs. One single GAIA board can control up to 10 V_d and 10 V_g and monitor 10 V_d, 10 V_g and 10 drain currents (10 I_d). The I_d of each LNA module amplification stage is imposed by the assigned V_d and V_g. The digital board is designed to provide high bias voltage stability and proved to generate very low RFI emission, as required for radio astronomy purposes.

The Dewar control board performs the monitoring of the cryogenic temperatures, of the cryostat vacuum pressure and the control management of the cryo board, while the cryo board controls the vacuum valve (on/off), the primary vacuum pump (on/off) and the cryocooler (on/off).

XI. CONCLUSION

We reported on an advanced feasibility study of a W-band cryogenic multibeam receiver for the Gregorian focus of the 64-m diameter Sardinia Radio Telescope. The instrument is a heterodyne focal plane array receiver operating between 70 and 116 GHz funded through a grant by the Italian Ministry of University and Research. Our receiver design study takes into account the shaping of the SRT antenna optics, which reduces the field of view and limits the usable area of the focal plane to a diameter of ≈130 mm at W band. We discussed possible alternative solutions of the receiver optics, and proposed various layouts for the cryogenic array, all based on dual-linear polarization feed-horns with orthomode transducers (OMT) and W-band HEMT low noise amplifier (LNA) technology suitable to cover the 70-116 GHz band.

Our proposed solution for the optical system is an array located on the focal plane without re-imaging optics: the array can adopt either a 3 × 3 configuration (9 dual-polarization pixels) and non-miniaturized single-pixel footprint, where components utilize standard UG387 waveguide flanges, or a 4 × 4 configuration (16 dual-polarization pixels) and miniaturized single-pixel footprint, where components require non-standard waveguide flanges. We described the preliminary design of all the cryogenic elements of the receiver chain, including feed-horn, OMT and LNA modules in relation to their footprint dimension and critically discuss their required mechanical and electrical specifications and RF performance.

The core technology is based on miniaturized receiver modules that would be amenable to automated assembly. We illustrated the architecture and preliminary details of the 4 × 4 cryogenic receiver array, our design goal for the instrument. A novel scalable approach to building a focal plane array was presented. The array is located inside a vacuum vessel and cryogenically cooled to ≈20 K by a commercial closed-cycle refrigerator. The down-converter for the receiver array consists of four four-pixel modules located at room temperature, outside the cryostat. We use a sideband separation (2SB) down-conversion scheme with 4-12 GHz IF delivering two independent sidebands, USB and LSB, for each pixel/polarization, i.e. 64 × IF outputs (16 pixels × 2 polarizations × 2 sidebands). An IF selector halves the number of IF output signals to 32 to allow their transportation to the backend through RFoF fiber optics links (38 available). A mechanical derotator will track the parallactic angle. Our preliminary estimates demonstrate that the 4×4 receiver array can be made to deliver high antenna efficiency ($\eta_{\rm eff}$ ≥0.50 excluding Ruze RMS surface errors, focus, radiation efficiency, and blockage), low noise (SSB noise $T_{\rm rec,SSB}$ ≈50 K) and high image sideband rejection ($R_{\rm i}$ >10 dB) across the 70-116 GHz RF band and with 4-12 GHz IF band. The instantaneous FoV covered by the 4 × 4 array will be ≈2.3 × 2.3 arcmin^2, unfilled, with separation between contiguous elements of 43 arcsec. Various combinations of observing modes will be possible for scientific observation of weak radio astronomy sources and of the Sun. Astronomers will be able to select 32 × (4-12 GHz) IF signals from the receiver outputs, and choose among LSB, USB, Pol-H and Pol-V, which combination will be delivered to the backend.

The development of the instrument has been contracted by INAF to UKRI following an international call for tenders. The receiver will utilize the Monitor and Control unit and the build-to-print mechanical derotator developed by INAF. The receiver will enable astronomical imaging of radio astronomy sources at high mapping speeds with ≈12 arcsec angular resolution over the 70-116 GHz band allowing to carry out state-of-the-art science studies.

APPENDIX A: 3 × 3 ARRAY

3 × 3 ARRAY CONFIGURATION AND BEAMS PROJECTED ON THE SKY

The simplest layout of an array that fulfills the minimum requirements described in Section III consists of nine dual-linear polarization feeds arranged in a square 3 × 3 configuration placed at the Gregorian focus, without re-imaging optics, like the one shown in the left panel of Fig. 25. The dashed circle on the array layout indicates the points at a distance d ≈63 mm from the optical axis on the focal plane, where the antenna gain is 0.6 dB below the on-axis gain at 100 GHz. We performed the electromagnetic simulations of such optical system with the Grasp software at four representative frequencies in the band of interest (70, 93, 100, and 116 GHz) for the on-axis feed (feed n. 1 in Fig. 25), for the side feeds (feeds n. 2, 4, 6, and 8), and for the corner feeds (feeds n. 3, 5, 7, and 9). The results are listed in Tab. A1. These simulations assumed the ideal SRT-shaped surfaces of the primary and secondary mirrors with no surface errors and the array placed at the Gregorian focus. We used the GTD (Geometrical Theory of Diffraction) method to model the scattering of the secondary mirror, and the PO (Physical Optics) method to model the scattering of the primary reflector. The modeling accounts for the radiation patterns of an illuminating diffraction-limited feed-horn optimized for operation across the full 70-116 GHz bandwidth. At 93 GHz, the central frequency of the 70-116 GHz band, the loss of the antenna gain for the corner feeds is approximately 10% of the on-axis value. This loss is 18.5 % at 116 GHz and 4.7% at 70 GHz.

The HPBW footprint locations of the projected beams on the sky for this simple 3×3 optical configuration are shown in the right panel of Fig. 25. The frequency-independent beam separation is ≈62 arcsec. This angular separation corresponds to 5.3 HPBW at 116 GHz, where HPBW≈11.6 arcsec, and to 4 HPBW at 70 GHz, where HPBW≈ 15.2 arcsec (these values refer to the central pixel). Fig. 26 shows possible scanning geometries for the 3 × 3 configuration that could be used for mapping large angular areas on the sky at three frequencies: 70 GHz, 93 GHz and 116 GHz. An almost Nyquist-sampling is achieved at all frequencies with three sub-scans. The profiles shown on the left of each panel represent the overlapping level of all the combined beams.

FOOTPRINT SIZE OF SINGLE PIXEL FEED AND ARRANGEMENTS OF CRYOGENIC 3 × 3 ARRAY

A feed spacing of ≈45 mm, illustrated in the left panel of Fig. 25, would allow accommodating two standard UG387 waveguide flanges side by side, as alignment pins and screw holes of one such flange are located on a 19.05 mm diameter. An array consisting of 3 × 3 feeds with spacing between contiguous elements of ≈45 mm (maximum footprint size ≈45 × 45 mm^2) can fit inside the ≈63 mm FoV radius. Models of one possible configuration of the 3 × 3 cryogenic array, with feed spacing corresponding to the illustration in the left panel of Fig. 25, are shown in Fig. 27. The 3D sketches of the array utilize the representative images of the ALMA Band 2+3 component feature sizes, as from Fig. 11. Although a 3 × 3 array with standard waveguide flanges could fit into a ≈130 mm diameter footprint, it is desirable to reduce the feed spacing below ≈45 mm to achieve high antenna efficiency of the off-axis beams, reduce the optical aberrations of the off-axis beams, and decrease the beam spacing in the sky. Fig. 28 shows an example of a different method for implementing the passive parts (feed and OMT) for an optimized 3 × 3 array configuration minimizing the element separation to ≈36 mm on the focal plane, with the corner feed aperture center laying on a ≈102 mm diameter circle. The layout requires the development of non-commercial LNAs with a suitable footprint that fit behind the OMT, similar to those presented in Sec. VI.

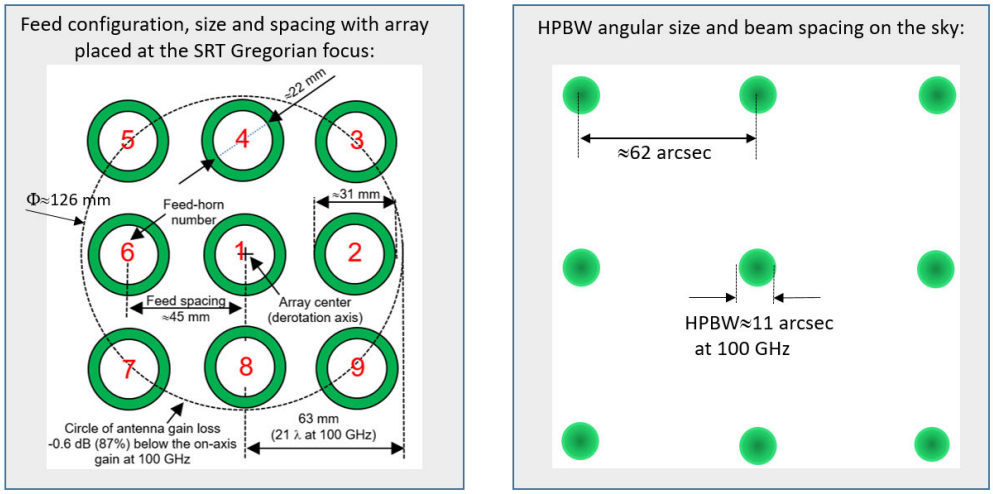

FIGURE 25. Left: Configuration of a 3 × 3 array on the SRT Gregorian focal plane with 45 mm spacing between contiguous feeds. The diameter of the feed aperture is about 22 mm. Right: Sketch of 3 × 3 beams projected on the sky showing the angular separation between contiguous beams (62 arcsec) and the HPBW≈11 arcsec of each beam at 100 GHz. The plate scale factor on the focal plane is 1.4 arcsec/mm. The example refers to an array of feeds placed on the Gregorian focus without re-imaging optics.

TABLE 8. Optical parameters of the 3 × 3 multifeed with 45 mm feed spacing of Fig. 25 illuminating the srt from the gregorian focus simulated with the grasp software. Feed numbering: n. 1, central feed; n. 2, 4, 6 8, near-center feeds; n. 3, 5, 7, 9 corner feeds. ruze rms surface errors, focus, radiation efficiency, and blockage, are not considered in the calculation of the antenna efficiency.

	Feed number (see Fig. A1)	70 GHz	93 GHz	100 GHz	116 GHz
Gain CoPolar [dBi]	1	91.50	94.68	95.02	95.14
	2, 4, 6, 8	91.38	94.42	94.71	94.62
	3, 5, 7, 9	91.27	94.19	94.44	94.20
3dB BeamWidth [arcsec]	1	15.23	12.38	11.95	11.59
	2, 4, 6, 8	15.19	12.35	11.88	11.30
	3, 5, 7, 9	15.08	12.20	11.74	11.27
Angular offset from optical axis θ [arcsec]	1	0.00	0.00	0.00	0.00
	2, 4, 6, 8	62.24	62.07	61.98	61.65
	3, 5, 7, 9	87.96	87.80	87.72	87.42
Antenna efficiency $\eta_{eff}=\eta_t\,\eta_s\,\eta_p$	1	0.64	0.76	0.71	0.54
	2, 4, 6, 8	0.62	0.71	0.66	0.48
	3, 5, 7, 9	0.61	0.68	0.62	0.44
Gain loss with respect to illumination with central feed [%]	1	0.0	0.0	0.0	0.0
	2, 4, 6, 8	3.1	6.6	7.0	11.1
	3, 5, 7, 9	4.7	10.5	12.7	18.5
Cross-polarization level [dB]	1	-48.82	-39.22	-38.33	-35.73
	2, 4, 6, 8	-43.67	-38.67	-37.91	-34.84
	3, 5, 7, 9	-47.85	-38.43	-37.55	-34.16

APPENDIX B: IFS SELECTOR

An multibeam receiver, is needed to halve the number of 64 available IF signals at the cryostat output and extract 32 IFs for transportation to the data processing center. The IFs selector allows choosing any of four possible combinations described in Section III. A block diagram of the IFs selector is shown in Fig. 29: the top panel illustrates the circuitry and interconnections for the IFs selection of one dual-polarization 2SB receiving feed, based on a single transfer switch and two Single Pole Double Throw (SPDT) switches, while the bottom panel illustrates a diagram of the full 16-pixel array IF switch matrix.

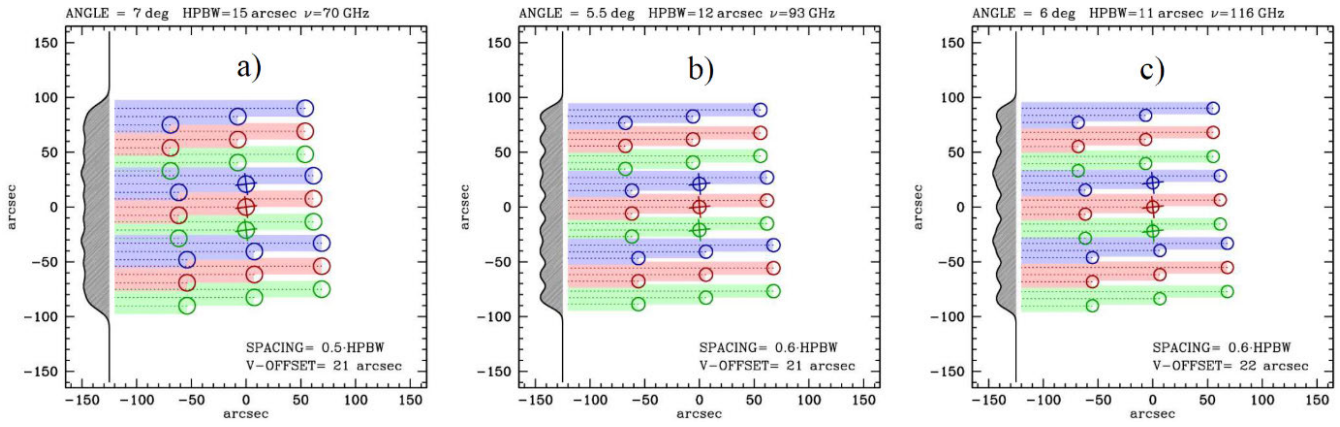

FIGURE 26. Scanning geometry with the 3x3 array for mapping with respect to the scanning direction at 70 GHz (left, "a"), 93 GHz (center, "b") and 116 GHz (right, "c"). Near-Nyquist sampling is achieved with three sub-scans. The overlapping of the beams is shown on the left of each panel.

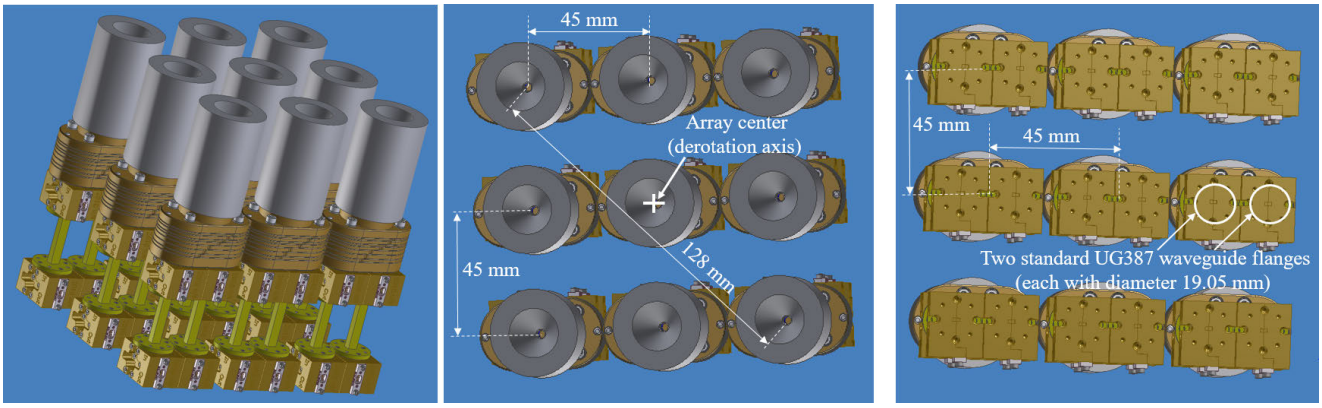

FIGURE 27. 3D sketch of 3 × 3 cryogenic array based on the ALMA Band 2+3 chain: view of fully assembled array with feed, OMT and LNA modules (left panel). Front view (center panel) and back view (right panel) of 3 × 3 W-band dual-cryogenic receiver array showing, respectively the feed-horn apertures and the 18 (9 pixels × 2 polarizations) waveguide outputs of the LNA modules. The separation between the axis of opposite corner feeds is approximately 128 mm.

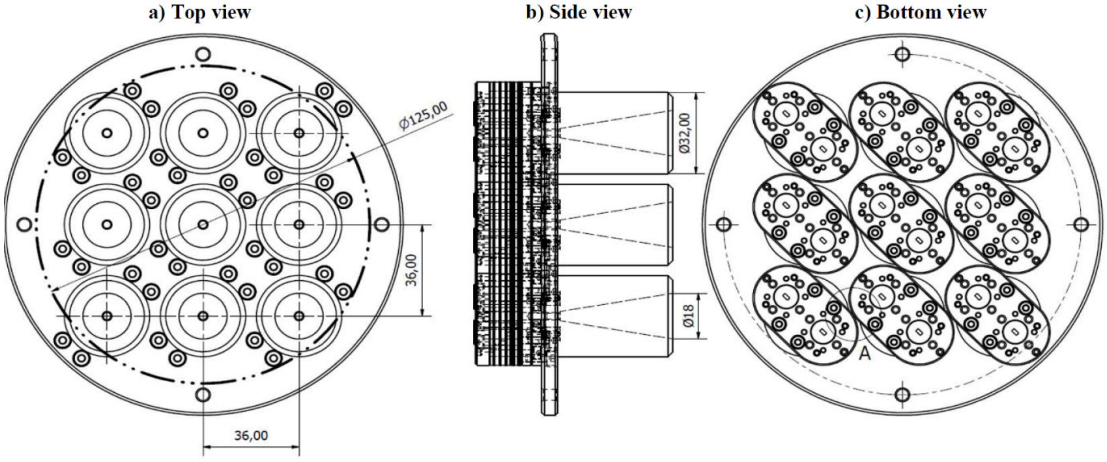

FIGURE 28. Possible arrangement of the 3x3 array based on feed cascaded with ALMA Band 2+3 OMT designed by INAF (top view, "a", left panel; side view, "b", center panel, bottom view, "c", right panel). The oval-shaped OMTs (cross-section maximum dimensions ≈25.5 × 44.5 mm2) are oriented at 45 degrees to the horizontal plane to maximize the filling factor of the focal plane. The E-planes of the WR10 waveguide outputs of each OMT are parallel. The separation of contiguous feeds is 36 mm and the axis of the feeds are confined within a diameter of ≈102 mm. The INAF feed-horn and OMT designs for the SRT W-band array (see Fig. 11 left), adapted from ALMA Band 2+3, have a footprint of only 31 mm, smaller than the one shown.

APPENDIX C: RE-IMAGING OPTICS

A re-imaging optics located in front of the W-band array of feed-horns would allow:

a) to achieve a frequency-independent sub-reflector illumination, with optimum high antenna efficiency obtained with an edge taper value of ≈-12 dB;

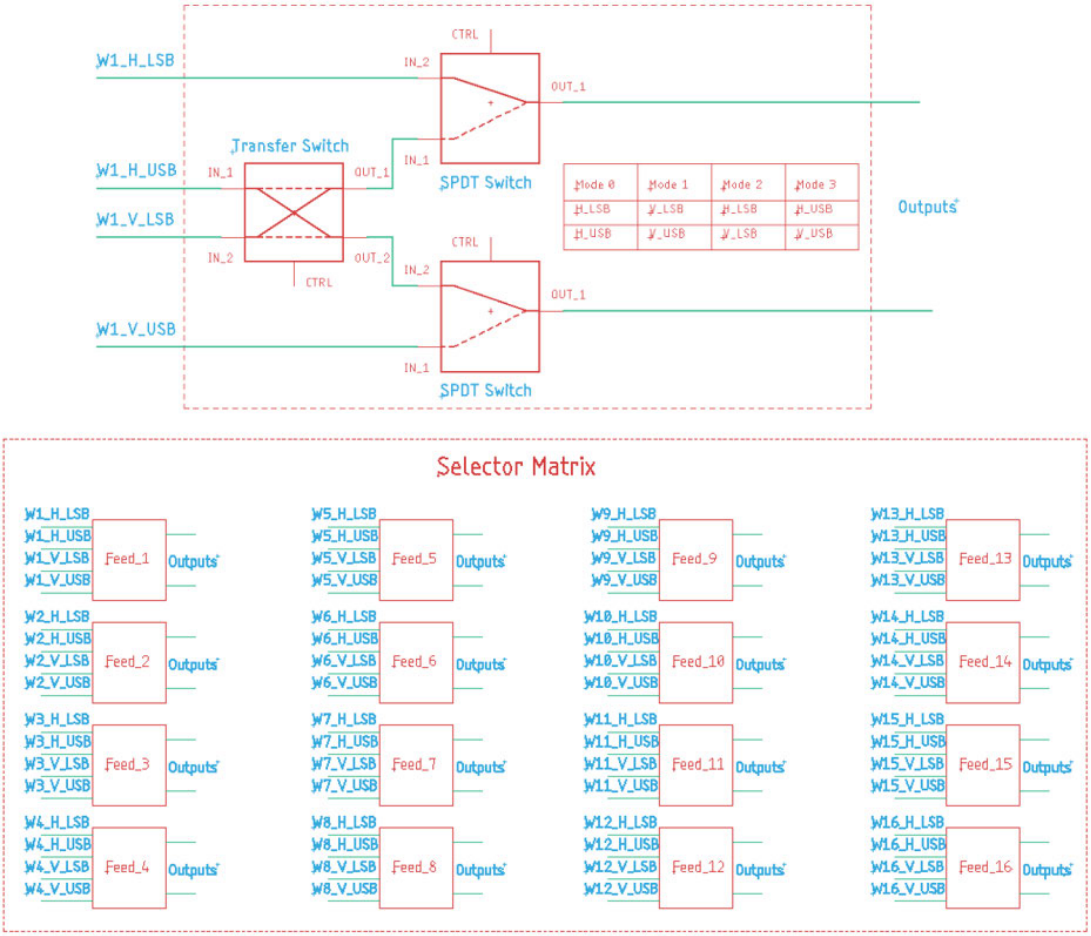

FIGURE 29. Top: Block diagram of the IF selector for one dual-polarization 2SB feed with four IF input signals and two IF output signals. The single selector utilizes one transfer switch and two SPDT switches. Bottom: Block diagram for the full selector matrix of the 16-element array with 64 IF inputs and 32 IF outputs.

b) to transform a suitable spacing between feed-horns into a $\approx 2.5\times$ HPBW spacing in the Gregorian focal plane, without requiring miniaturization of the single-pixel feed-system footprint. This transformation achieves the minimum angular confinement of the projected beams without loss of optical efficiency (specified maximum $5.7 \times$ HPBW);
c) to reduce the size of the vacuum window and IR filter, thus decreasing both its thickness (and consequently its insertion losses and added noise) and the infrared thermal loading on the cryogenic stages;
1) to maximize the coupling between each feed-horn and the telescope.

However, it would be challenging to confine such a high-performance re-imaging optics in the cold cryostat (or in front of it) ahead of the W-band feed-horn array due to the mechanical constraints imposed by the limited dimensions available at the SRT Gregorian focus, as full front-end instrument must also include a mechanical derotator and cable-wrap assembly that takes up a large fraction of space in the axial direction. Also, the re-imaging optics system should guarantee high performance and induce negligible optical aberrations when coupled to the shaped telescope primary and secondary mirrors (negligible truncation loss, beam distortion, beam squint, insertion loss, cross-polarization, etc.).

APPENDIX D: POSSIBLE ARCHITECTURE OF CRYOGENIC RECEIVER CHAIN

The final architecture of the cryogenic receiving chain might adopt different configurations, for example employing:

1) an isolator in place of the short waveguide section (to decrease the standing waves and improve matching), or a direct cascade of the two LNA modules with no interconnecting waveguides;
2) a second stage high-IP1dB LNA at room temperature (rather than two cryogenic LNA modules);
3) a single LNA module for both polarization channels in cascade to the OMT (dual-polarization LNA);
4) an ''active OMT'' that incorporate LNAs in a dual polarization module.

APPENDIX E: MITIGATION TECHNIQUES TO AVOID RECEIVER SATURATION DURING SUN OBSERVATION

Various solutions can be used to mitigate a possible compression of the receiver chain during Sun observations, which would otherwise lead to operations in the non-linearity

regime. These solutions, all of which inevitably impact the receiver noise performance, include the following:

a) drive the last LNA stage to a higher current to achieve higher output P1dB (≈0 dBm). This is only possible if the amplifier gain does not increase with the driving current;
b) use a single cryogenic LNA or two cascaded cryogenic LNAs with total gain not greater than 33 dB, enough to reduce the noise of the following receiver stages to a negligible level while avoiding signal compression: the cryogenic amplifier(s) could be either cascaded with a room temperature LNA with high P1dB followed by a room temperature down-converter, or by a low-noise low-conversion loss down-converter to be located at room or cryogenic temperature;
c) reduce the RF input bandwidth injected into the W-band LNAs chain using a quasi-optical band pass filter at the receiver input, in front of the vacuum window, as for the proposed solution shown in Figs. 19 and 21. The room-temperature quasi-optical filter reduces the input bandwidth by one order of magnitude (from ≈60 GHz to ≈6 GHz). It is switched in the RF signal path only for solar observations. The equivalent noise temperature added by this passive component, which scales with its estimated insertion loss IL < 0.7 dB (>85% transmission) across the filter bandpass, is expected to be ≈50 K. The receiver noise at the input of the quasi-optical band pass filter would be $T_{\mathrm{rec,SSB}}$ ≈122 K, having assumed the receiver noise in front of the vacuum window is 60 K;
d) attenuate the RF input signal injected into the LNAs chain using a broadband quasi-optical attenuator at the receiver input, in front of the vacuum window. The room-temperature quasi-optical attenuator is designed to reduce the input power of ≈5 dB (equivalent added noise ≈627 K). It is switched in the RF signal path only for solar observations. The receiver noise at the input of the quasi-optical attenuator would be $T_{\mathrm{rec,SSB}}$ ≈820 K, having assumed the receiver noise in front of the vacuum window is 60 K;
e) attenuate the RF input signal injected into the LNAs chain using a cryogenic broadband variable waveguide attenuator operating at ≈20 K in front of the LNAs. The variable attenuator should be remotely controlled to attenuation values in the range ≈0–15 dB, and designed with low insertion loss when set for 0 dB attenuation, to have minimum impact on the receiver noise performance during weak radio astronomy source observations. When set for 10 dB attenuation, the equivalent added noise of the cryogenic attenuator would be ≈180 K. The receiver noise at the input of the vacuum window with attenuation set to 10 dB would be $T_{\mathrm{rec,SSB}}$ ≈820 K, having assumed the receiver noise with no attenuation is 60 K;
f) de-tune the LNA bias to reduce its gain (see Sec. X).

We decided to adopt solutions c) and f), the latter being required for solar flare observations.

REFERENCES

[1] G. Grueff, G. Alvito, R. Ambrosini, P. Bolli, A. Maccaferri, G. Maccaferri, M. Morsiani, L. Mureddu, V. Natale, L. Olmi, A. Orfei, C. Pernechele, A. Poma, I. Porceddu, L. Rossi, and G. Zacchiroli, "Sardinia Radio Telescope: The new Italian project," *Proc. SPIE*, vol. 5489, pp. 773–783, Jun. 2004.

[2] G. Tofani *et al.*, "Status of the Sardinia Radio Telescope project," *Proc. SPIE*, vol. 7012, Jun. 2008, Art. no. 70120F.

[3] I. Prandoni *et al.*, "The Sardinia radio telescope: From a technological project to a radio observatory," *Astron. Astrophys.*, vol. 608, p. A40, Dec. 2017, doi: 10.1051/0004-6361/201630243.

[4] P. Bolli *et al.*, "Sardinia radio telescope: General description, technical commissioning and first light," *J. Astronomical Instrum.*, vol. 4, nos. 3–4, Dec. 2015, Art. no. 1550008, doi: 10.1142/S2251171715500087.

[5] G. Valente, T. Pisanu, P. Bolli, S. Mariotti, P. Marongiu, A. Navarrini, R. Nesti, and A. Orfei, "The dual-band LP feed system for the Sardinia Radio Telescope prime focus," *Proc. SPIE*, vol. 7741, Jul. 2010, Art. no. 774126.

[6] A. Orfei, A. Cattani, M. Poloni, J. Roda, S. Mariotti, A. Maccaferri, A. Orlati, and A. Scalambra, "Caratterizzazione del ricevitore nella banda 5.7-7.7 GHz," INAF SRT Memo Ser., Bologna, Italy, Tech. Rep. GAI04 FR 5.0, May 2011.

[7] A. Orfei, L. Carbonaro, A. Cattani, A. Cremonini, L. Cresci, F. Fiocchi, A. Maccaferri, G. Maccaferri, S. Mariotti, J. Monari, M. Morsiani, V. Natale, R. Nesti, D. Panella, M. Poloni, J. Roda, A. Scalambra, and G. Tofani, "A multi-feed receiver in the 18 to 26.5 GHz band for radio astronomy," *IEEE Antennas Propag. Mag.*, vol. 52, no. 4, pp. 62–72, Aug. 2010, doi: 10.1109/MAP.2010.5638236.

[8] A. Navarrini *et al.*, "The Sardinia Radio Telescope front-ends," in *Proc. 27th Int. Symp. Space THz Tech. (ISSTT)*, Nanjing, China, Apr. 2016, pp. 1–4.

[9] A. Navarrini *et al.*, "Front-ends and phased array feeds for the Sardinia Radio Telescope," in *Proc. 32nd URSI GASS*, Montreal, QC, Canada, Aug. 2017, pp. 1–4.

[10] A. Pellizzoni, S. Righini, G. Murtas, F. Buffa, R. Concu, E. Egron, M. N. Iacolina, S. Loru, A. Maccaferri, A. Melis, A. Navarrini, A. Orfei, P. Ortu, T. Pisanu, A. Saba, G. Serra, G. Valente, A. Zanichelli, P. Zucca, and M. Messerotti, "Imaging of the solar atmosphere in the centimetre-millimetre band through single-dish observations," *Il Nuovo Cimento*, vol. 42, no. 1, pp. 1–4, 2019, doi: 10.1393/ncc/i2019-19009-x.

[11] G. Muntoni, L. Schirru, T. Pisanu, G. Montisci, G. Valente, F. Gaudiomonte, G. Serra, E. Urru, P. Ortu, and A. Fanti, "Space debris detection in low Earth orbit with the Sardinia radio telescope," *Electronics*, vol. 6, no. 3, p. 59, Aug. 2017, doi: 10.3390/electronics6030059.

[12] F. Buffa, G. Serra, P. Bolli, A. Fara, G. L. Deiana, F. Nasir, C. Castiglia, and A. M. S. Delitala, "K-band system temperature forecast for the Sardinia radio telescope," INAF, Cagliari, Italy, Tech. Rep. 54, Apr. 2016. [Online]. Available: http://eonstore.oa-cagliari.inaf.it/fbuffa/report/

[13] F. T. Nasir, C. Castiglia, F. Buffa, G. L. Deiana, A. Delitala, and A. Tarchi, "Weather forecasting and dynamic scheduling for a modern cm/mm wave radiotelescope," *Experim. Astron.*, vol. 36, nos. 1–2, pp. 407–424, Aug. 2013.

[14] A. Navarrini, L. Olmi, R. Nesti, F. Buffa, and A. Orlati, "Estimates of system noise temperature in W-band at SRT and effects of beam truncation due to the Gregorian radome," INAF, Cagliari, Italy, Tech. Rep., 63, 2020. [Online]. Available: http://hdl.handle.net/20.500.12386/28787

[15] A. Ladu, T. Pisanu, A. Navarrini, P. Marongiu, and G. Valente, "A 3 mm band SIS receiver for the Sardinia Radio Telescope," *Proc. SPIE*, vol. 9153, Jun. 2014, Art. no. 91532J, doi: 10.1117/12.2056339.

[16] A. Ladu, P. Ortu, A. Saba, P. Marongiu, G. Valente, T. Pisanu, E. Urru, A. Navarrini, and G. Mazzarella, "The control system and the new cryogenics of the 3 mm band SIS receiver for the Sardinia radio telescope," *Proc. SPIE*, vol. 9914, p. 75, Jul. 2016.

[17] A. Navarrini, "Sviluppi di Ricevitori e di Componentistica per Banda 3 mm ad INAF-OA Cagliari," in *Proc. 4th Workshop Sull'Astronomia Millimetrica in Italia*, Bologna, Italy, Nov. 2017, p. 12, doi: 10.5281/zenodo.1116242. [Online]. Available: https://zenodo.org/record/1116242#.YAh6z-hypha

[18] A. Orfei, M. Morsiani, G. Zacchiroli, G. Maccaferri, J. Roda, and F. Fiocchi, "Active surface system for the new Sardinia Radio Telescope," *Proc. SPIE*, vol. 5495, pp. 116–125, Jun. 2004, doi: 10.1117/12.548944.
[19] A. Navarrini, L. Olmi, R. Nesti, P. Marongiu, P. Ortu, L. Cresci, A. Orlati, A. Scalambra, and A. Orfei, "Design concept of W-band multibeam receiver for the SRT," in *Proc. 31st IEEE Int. Symp. Space THz Technol.*, Tempe, AZ, USA, Mar. 2020, pp. 1–3.
[20] F. Govoni *et al.*, "The high-frequency upgrade of the Sardinia Radio Telescope," in *Proc. URSI GASS*, Rome, Italy, Aug. 2021, pp. 1–4, doi: 10.23919/URSIGASS51995.2021.9560570.
[21] L. Morgan, W. Armentrout, D. Frayer, F. Lockman, N. Butterfield, A. Minter, K. O'Neal, and P. Salas, "Argus-144: High resolution molecular gas mapping with a 144-element W-band array on the green bank telescope," *Bull. AAS*, vol. 53, no. 6, p. 326, Jun. 2021.
[22] M. Sieth *et al.*, "Argus: A 16-pixel millimeter-wave spectrometer for the Green Bank Telescope," *Proc. SPIE*, vol. 9153, Jun. 2014, Art. no. 91530P, doi: 10.1117/12.2056339.
[23] N. R. Erickson, R. M. Grosslein, R. B. Erickson, and S. Weinreb, "A cryogenic focal plane array for 85–115 GHz using MMIC preamplifiers," *IEEE Trans. Microw. Theory Techn.*, vol. 47, no. 12, pp. 2212–2219, Dec. 1999, doi: 10.1109/22.808962.
[24] T. Nakajima *et al.*, "Development of a new multi-beam array 2SB receiver in 100 GHz band for the NRO 45-m radio telescope," in *Proc. 23rd Int. Symp. Space THz Tech. (ISSTT)*, Tokyo, Japan, Apr. 2012, pp. 100–103.
[25] T. Minamidani *et al.*, "Development of the new multi-beam 100 GHz band SIS receiver FOREST for the Nobeyama 45-m Telescope," *Proc. SPIE*, vol. 9914, Jul. 2016, Art. no. 99141Z.
[26] P. Bolli *et al.*, *An International Survey of Front-End Receivers and Observing Performance of Telescopes for Radio Astronomy*. El Paso, TX, USA: PASP, Publications of the Astronomical Society of the Pacific, Aug. 2019.
[27] A. Orfei, A. Scalambra, P. Marongiu, M., Poloni, G., Comoretto, A. Navarrini, A. Orlati, and E. Carretti, "Nuovo sistema ricevitori a SRT e loro integrazione AI back-end," INAF Internal Rep., Bologna, Italy, Tech. Rep. 11, 2020. [Online]. Available: http://hdl.handle.net/20.500.12386/23454
[28] *Xilinx Virtex-7 FPGA-Based Square Kilometer Array Reconfigurable Application Board (SKARAB)*. Accessed: Feb. 20, 2022. [Online]. Available: https://casper.berkeley.edu/
[29] *Xilinx Radio Frequency System on Chip (RFSoC) Technology*. Accessed: Feb. 20, 2022. [Online]. Available: https://www.xilinx.com/products/silicon-devices/soc/rfsoc.html
[30] W. Alef, G. Tuccari, S. Dornbusch, M. Wunderlich, A. Roy, H. Rottmann, J. Wagner, R. Haas, and K.-Å.-L. Johansson, "DBBC3 the new wide-band backend for VLBI," in *Proc. 14th Eur. VLBI Netw. Symp. Users Meeting PoS(EVN)*, Feb. 2019, pp. 8–11.
[31] *ROACH-1 Digital Filter Bank (Version 1 of Reconfigurable Open Architecture Computing Hardware)*. Accessed: Feb. 20, 2022. [Online]. Available: https://casper.berkeley.edu/
[32] A. Melis *et al.*, "SArdinia Roach2-based digital architecture for radio astronomy (SARDARA)," *J. Astronomical Instrum.*, vol. 7, no. 1, Mar. 2018, Art. no. 1850004, doi: 10.1142/S2251171718500046.
[33] A. Melis, D. Perrodin, N. Antonietti, M. Burgay, R. C. C. Maccone, E. S. M. Montebugnoli, A. Navarrini, P. Pari, M. Pilia, and A. Possenti, "Involvement of the Sardinia Radio Telescope in the breakthrough listen initiatives," in *The Search for ExtraTerrestrial Intelligence. Springer Proceedings in Physics*, vol. 260. Cham, Switzerland: Springer, 2021, doi: 10.1007/978-3-030-63806-1_10.
[34] T. Pisanu, L. Schirru, E. Urru, and P. Maxia, "Status of the Sardinia Radio Telescope as a receiver of the BIRALET radar for space debris observations," *Proc. SPIE*, vol. 11445, Dec. 2020, Art. no. 114457B, doi: 10.1117/12.2576249.
[35] R. Madde, T. Morley, M. Lanucara, R. Abello, M. Mercolino, J. D. Vicente, and G. M. A. Sessler, "A common receiver architecture for ESA radio science and delta-DOR support," *Proc. IEEE*, vol. 95, no. 11, pp. 2215–2223, Nov. 2007, doi: 10.1109/JPROC.2007.905184.
[36] G. Valente, M. N. Iacolina, S. Viviano, A. Saba, G. Serra, G. Parca, G. Impresario, G. D'Amore, S. W. Asmar, G. Montisci, P. Ortu, D. Perrodin, F. Gaudiomonte, and A. Melis, "Sardinia deep space antenna: Current program status and results," in *Proc. 70th Int. Astron. Congr., (IAC)*, Washington, DC, USA, Oct. 2019, pp. 21–25.
[37] G. Serra, P. Bolli, G. Busonera, Pisanu, S. Poppi, F. Gaudiomonte, G. Zacchiroli, J. Roda, M. Morsiani, and J. López-Pérez, "The microwave holography system for the Sardinia radio telescope," *Proc. SPIE*, vol. 8444, Sep. 2012, Art. no. 84445W, doi: 10.1117/12.926160.
[38] P. Bolli, F. Gaudiomonte, R. Ambrosini, C. Bortolotti, and M. Roma, "The receiving system of the mobile laboratory for RFI measurements," INAF-OAC, Cagliari, Italy, Internal Rep. 20, Aug. 2012. [Online]. Available: https://www.oa-cagliari.inaf.it/area.php?page_id=10&skip=5
[39] F. L. Schöier, F. F. S. van der Tak, E. F. van Dishoeck, and J. H. Black, "An atomic and molecular database for analysis of submillimetre line observations," *Astron. Astrophys.*, vol. 432, no. 1, pp. 369–379, Mar. 2005.
[40] M. Heyer and T. M. Dame, "Molecular clouds in the milky way," *Annu. Rev. Astron. Astrophys.*, vol. 53, no. 1, pp. 583–629, Aug. 2015.
[41] L. Olmi, "The detection of high-redshift CO lines using the SRT," in *Proc. SRT Conf.*, vol. 1, 2002, pp. 83–90.
[42] C. Plainaki, M. Antonucci, A. Bemporad, F. Berrilli, B. Bertucci, M. Castronuovo, P. D. Michelis, M. Giardino, R. Iuppa, M. Laurenza, F. Marcucci, M. Messerotti, L. Narici, B. Negri, F. Nozzoli, S. Orsini, V. Romano, E. Cavallini, G. Polenta, and A. Ippolito, "Current state and perspectives of space weather science in Italy," *J. Space Weather Space Climate*, vol. 10, p. 6, Feb. 2020.
[43] M. Marongiu, A. Pellizzoni, S. Mulas, and G. Murtas, "A Python approach for solar data analysis: SUNDARA (SUNDish Active Region Analyser), preliminary development," INAF, Washington, DC, USA, Tech. Rep., 81, Mar. 2021. [Online]. Available: http://hdl.handle.net/20.500.12386/30719
[44] L. Olmi, "Future 3-mm receivers for the SRT," *Memorie della Societá Astronomica Italiana Supplementi*, vol. 10, p. 40, Jan. 2006.
[45] J. Baars, "Characteristics of a reflector antenna: Parameters, graphs and formulae for Cassegrain systems with mathematica expressions for numerical computation," ALMA Memo, Orlando, FL, USA, Tech. Rep., 456, Apr. 2003.
[46] L. Olmi and P. Bolli, "Ray-tracing and physical-optics analysis of the aperture efficiency in a radio telescope," *Appl. Opt.*, vol. 46, pp. 4092–4101, Jul. 2007.
[47] O. Garnier, A. Navarrini, F. Schaefer, P. Serres, F. Thome, and S. Turk, "Multipixel W-band FPA demonstrator composed of cryogenic module and down conversion module," AETHRA WP5.1 Semicond. LNAs MMIC Receiv., Brasília, Brazil, Tech. Rep. H2020-INFRAIA-2016-2017/H2020-INFRAIA-2016, Jan. 2021. [Online]. Available: https://radiowiki.mpifr-bonn.mpg.de/lib/exe/fetch.php?media=jra:730562_radionet-d5.3_210129.pdf
[48] G. Dulk, "Solar radio emissions," in *Proc. 5th Int. Workshop Held Graz Austria*, H. O. Rucker, M. L. Kaiser, and Y. Leblanc, Eds. Vienna, Austria: Austrian Academy of Sciences Press, Apr. 2001, p. 429.
[49] M. Loukitcheva, "First solar observations with ALMA," *Adv. Space Res.*, vol. 63, no. 4, pp. 1396–1403, Feb. 2019.
[50] C. Chiong, P. Chiang, Y. Hwang, and Y. Huang, "Strategies on solar observation of Atacama large millimeter/submillimeter array (ALMA) band-1 receiver," *Proc. SPIE*, vol. 9914, Jul. 2016, Art. no. 991421.
[51] P. F. Goldsmith, "Sub-millimeter heterodyne focal-plane arrays for high-resolution astronomical spectroscopy," *URSI Radio Sci. Bull.*, vol. 2017, no. 362, pp. 53–73, Sep. 2017.
[52] A. Navarrini and R. L. Plambeck, "A turnstile junction waveguide orthomode transducer," *IEEE Trans. Microw. Theory Techn.*, vol. 54, no. 1, pp. 272–277, Jan. 2006, doi: 10.1109/TMTT.2005.860505.
[53] A. Navarrini and R. Nesti, "Backward coupler waveguide orthomode transducer for 84–116 GHz," in *Proc. 19th Int. Symp. Space THz Technol.*, Groningen, The Netherlands, Apr. 2008, pp. 28–30.
[54] A. Navarrini and R. Nesti, "Symmetric reverse-coupling waveguide orthomode transducer for the 3-mm band," *IEEE Trans. Microw. Theory Techn.*, vol. 57, no. 1, pp. 80–88, Jan. 2009, doi: 10.1109/TMTT.2008.2008943.
[55] G. Valente, A. Navarrini, F. Schaefer, P. Serres, and F. Thome, "Architecture of highly integrated cryogenic active planar OrthoMode transducer for the 3-mm band," in *Proc. 2nd URSI Atlantic Radio Sci. Meeting (AT-RASC)*, May 2018, pp. 1–4.
[56] A. Navarrini and R. Nesti, "Characterization techniques of millimeter-wave orthomode transducers (OMTs)," *Electron.*, vol. 10, no. 15, p. 1844, 2021, doi: 10.3390/electronics10151844.
[57] R. Nesti, "ALMA band 2–3 feedhorn and OMT developments at INAF," presented at the ALMA Band 2+3 Workshop, Chalmers, Sweden, May 2016. [Online]. Available: https://www.chalmers.se/en/centres/GoCAS/Events/ALMA-Bands2and3-Workshop-2016/Documents/Nesti%20-%20ALMA%20Band%202-3%20Feedhorn%20and%20OMT%20developments%20at%20INAF.pdf
[58] P. Yagoubov *et al.*, "Wideband 67–116 GHz receiver development for ALMA band 2," in *Proc. A&A*, vol. 634, Feb. 2020, p. A46, doi: 10.1051/0004-6361/201936777.

[59] L. Olmi, "The optical design of relay optics for heterodyne millimeter-wave focal plane arrays," *Int. J. Infr. Millim. Waves*, vol. 21, no. 3, p. 365, 2000.
[60] F. Thome, F. Schafer, S. Turk, P. Yagoubov, and A. Leuther, "A 67–116-GHz cryogenic low-noise amplifier in a 50-nm InGaAs metamorphic HEMT technology," *IEEE Microw. Wireless Compon. Lett.*, early access, Dec. 22, 2021, doi: 10.1109/LMWC.2021.3134462.
[61] A. Navarrini, G. Valente, P. Serres, F. Schaefer, F. Thome, and O. Garnier, "Compact dual-polarization cryogenic receiver module for the 75–116 GHz band," in *Proc. Int. Conf. Electromagn. Adv. Appl. (ICEAA)*, Sep. 2018, pp. 479–482.
[62] F. Thome, E. Ture, A. Leuther, F. Schafer, A. Navarrini, P. Serres, and O. Ambacher, "A fully-integrated W-band I/Q-down-conversion MMIC for use in radio astronomical multi-pixel receivers," in *IEEE MTT-S Int. Microw. Symp. Dig.*, Aug. 2020, pp. 193–196.
[63] F. Thome, E. Ture, R. Iannucci, A. Leuther, F. Schafer, A. Navarrini, and P. Serres, "Frequency multiplier and mixer MMICs based on a metamorphic HEMT technology including Schottky diodes," *IEEE Access*, vol. 8, pp. 12697–12712, 2020, doi: 10.1109/ACCESS.2020.2965823.
[64] S. M. X. Claude, C. T. Cunningham, A. R. Kerr, and S.-K. Pan, "Design of a sideband-separating balanced SIS mixer based on waveguide hybrids," *ALMA Memo*, vol. 316, pp. 1–14, Sep. 2000.
[65] A. R. Kerr, S.-K. Pan, and J. E. Effland, "Sideband calibration of millimeter-wave receivers," ALMA Memo, Orlando, FL, USA, Tech. Rep. 357, Mar. 2001. [Online]. Available: http://legacy.nrao.edu/alma/memos/html-memos/alma357/memo357.pdf
[66] P. Ortu, A. Saba, G. Valente, F. Gaudiomonte, A. Navarrini, T. Pisanu, and E. Urru, "GAIA, Progettazione, realizzazione e caratterizzazione della GAIA board," INAF Internal Rep., Cagliari, Italy, Tech. Rep. 30, Jul. 2020. [Online]. Available: https://openaccess.inaf.it/handle/20.500.12386/26385
[67] P. Ortu, A. Saba, G. Valente, O. Garnier, P. Serres, F. Thome, F. Schaefer, and A. Navarrini, "Design of power stage of INAF Gaia board for biasing of AETHRA WP1 downconverter," INAF, Cagliari, Italy, Tech. Rep. 33, Jul. 2020. [Online]. Available: http://hdl.handle.net/20.500.12386/26502

A. NAVARRINI received the S.M. degree in physics from the University of Florence, Florence, Italy, in 1996, and the Ph.D. degree in electronics and microelectronics from Université Joseph Fourier, Saint Martin d'Hères, France, in 2002. He was with the Institut de Radioastronomie Millimétrique (IRAM), France, from 1998 to 2003, where he worked on the development of low-noise superconductor-insulator-superconductor receivers for the Atacama Large Millimeter Array (ALMA) and for the IRAM observatories. From 2003 to 2006, he was a Postdoctoral Fellow with the Radio Astronomy Laboratory, University of California, Berkeley, CA, USA, where he contributed to the development of the Combined Array for Research in Millimeter-wave Astronomy (CARMA) observatory. In 2006, he joined the National Institute for Astrophysics (INAF), Astronomical Observatory of Cagliari, Italy, to work on the instrumentation for the 64-m diameter Sardinia Radio Telescope (SRT). In parallel with his research commitment, he held a teaching position at the University of Cagliari. From 2010 to 2015, he was in charge of the Front-End Group at IRAM and developed the receivers for the Northern Extended Millimeter Array (NOEMA), France, and the IRAM 30-m diameter radio telescope at Pico Veleta, Spain. In 2015, he returned to the INAF-Astronomical Observatory of Cagliari, where he carries out research in low-noise microwave and millimeter-wave radio astronomy receivers, including multi beams and phased array feeds (PAF). He is the National Coordinator of the PAF activities at INAF in the framework of the Square Kilometer Array (SKA) Observatory Development Program (ODP). He is the Executive Director of the contract for the supply of the W-band multibeam receiver for the SRT.

L. OLMI was born in Florence, Italy, in 1961. He received the degree in physics and the Ph.D. degree in astronomy from the University of Florence, in 1987 and 1992, respectively. From 1993 to 1996, he was a Cornell University Research Associate with the Arecibo Observatory, Puerto Rico. From 1996 to 2001, he was a Senior Research Associate with the Astronomy Department, University of Massachusetts at Amherst, where he worked on the large millimeter telescope (LMT). From 1999 to 2010, he was a part of the international collaboration Balloon-borne Large Aperture Sub-millimeter Telescope (BLAST). Since 2001, he has been an Astronomer and a Technologist with the Istituto Nazionale di Astrofisica (INAF), Italy. From 2005 to 2017, he also shared a faculty position with the University of Puerto Rico. His research interests include the observation and analysis of molecular clouds and star forming regions, the effects of the atmosphere on radio astronomical observations, optical and EM design applied to radio telescopes and associated instrumentation, and novel instrumentation design for radio telescopes.

R. NESTI received the Laurea degree in electronics engineering and the Ph.D. degree in computer science and telecommunications from the University of Firenze, Italy, in 1996 and 2000, respectively. Since December 1999, he has been with the National Institute for Astrophysics, Arcetri Astrophysical Observatory, Firenze, where his main activity is in the area of radio astronomy receivers. His research interests include design and development of microwave passive devices for the receiver front-ends and numerical methods for the electromagnetic analysis and design of millimeter wave components.

P. ORTU was born in Nuoro, in October 1986. He received the bachelor's degree in electronic and telecommunications engineering from the University of Pisa, Pisa, Italy, in February 2013. He is currently pursuing the master's degree in electronics engineering with the University of Cagliari. He works at the National Institute for Astrophysics (INAF), Astronomical Observatory of Cagliari, Cagliari. His research interest includes analog and digital electronics implementation.

P. MARONGIU received the D.S.E.-Industrial Engineering Diploma degree in mechanics from the Sassari High School, Sassari, Italy, in 1995. For ten years, he worked in private companies, where he was responsible for mechanical production and quality control. Since 2009, he has been with the National Institute for Astrophysics (INAF), Astronomical Observatory of Cagliari, Italy, where he is currently involved in the development of receivers and is responsible for the mechanical and cryogenics for the Sardinia Radio Telescope (SRT).

A. ORLATI received the S.M. degree in mathematics and computer science from the University of Bologna, Italy, in 2000. From 2001 to 2004, he had a Research Fellowship with the National Council for Research (CNR). Since 2005, he has been a Technological Researcher at the National Institute for Astrophysics-Institute of Radio Astronomy (INAF-IRA). His activities are focused on technology development and management of ground-based facilities for radio astronomy. His major contributions are in control systems and data handling processing. He is currently in technical responsible or the radio telescope at Noto and an AIV Manager of the project ''The Enhancement of the Sardinia Radio Telescope for the study of the Universe at High Radio Frequencies.''

A. SCALAMBRA received the bachelor's degree in electronics from the Aldini Valeriani Institute, Bologna, in 1989. Since 2000, he has been working as an RF Technician at the Institute of Radioastronomy of Bologna, INAF. He is involved in the design and construction of radio astronomy receivers for the Italian radio telescopes. In particular, he works on systems for microwave RF signal conversion, including multi-beam and phased array feeds.

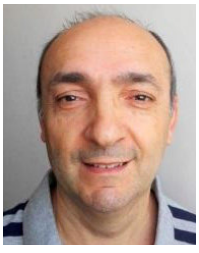

A. ORFEI received the S.M. degree in electronic engineering from Bologna University, Bologna, Italy, in 1983. He worked for three years at the G. Marconi Foundation Laboratories in the field of the fiber optics. Then for three years, he worked in a private company as a Design Engineer in the field of telecommunication. Since 1989, he has been a Researcher at the Institute of Radioastronomy (IRA)—National Council for Research, being in charge of all work concerning the very-long-baseline-interferometry (VLBI) 32m antenna at the Medicina Radio Observatory. This same work continued by changing affiliation to the Institute of Radioastronomy (IRA)—National Institute for Astrophysics, in 2005. He is currently the Head the of Microwave Receiver Group, IRA. His research interests include radio astronomy instrumentation, in particular low-noise microwave receivers, including multi beams and active surface systems for large reflector antennas.

J. RODA received the bachelor's degree in mechanics, in 1992. From 1993 to 1999, he worked in a private company. From 1999 to 2005, he was working at the Istituto di Radioastronomia—Consiglio Nazionale della Ricerche (IRA-CNR). Since 2005, he has been with the Istituto di Radiastronomia—Istituto Nazionale di Astrofisica (IRA-INAF), Medicina, Bologna, Italy. From 2006 to 2012, he was working on the construction and installation of the SRT 64-m antenna in Sardinia. His work focuses all aspects of structural and mechanical design.

A. CATTANI was born in 1962. He received the bachelor's degree in industrial electronics from ITIS O. Belluzzi, Bologna, Italy, in 1981. Since 1983, he has been working with the Institute of Radioastronomy at the Medicina Radio Observatory, Italy. Until 1997, he collaborated in the development of equipment for the control and data acquisition of the Northern Cross radio telescope, while in the following years, he collaborated in the realization of the JIVE European correlator, and then in the development of receivers for the Sardinia Radio Telescope (SRT). After 1997, he was involved in the development of the prototype instruments for the Low-Frequency Aperture Array for the Square Kilometer Array (SKA) built in Medicina. He is currently working on the control systems of the new receivers for the SRT and for the two 32-m diameter radio telescopes of Medicina and Noto, Italy. Furthermore, he is developing parts of the intermediate frequency (IF) distribution system for the SRT.

S. LEURINI received the S.M. degree in physics from the University of Cagliari, Italy, in 2001, and the Ph.D. degree in astronomy from the University of Bonn, Germany, in 2004. From 2005 to 2006, she was a Postdoctoral Fellow at the Max Planck Institute for Radioastronomy, Bonn, and then moved to the European Southern Observatory, Garching, as an ALMA Fellow, till 2009. From 2009 to 2016, she was an Astronomer at the Max Planck Institute for Radioastronomy. Since 2017, she has been a Researcher at INAF-Osservatorio Astronomico di Cagliari. Her research interests include star formation with major interest on the earliest stages of evolution massive stars and clusters.

F. GOVONI received the S.M. degree in physics and the Ph.D. degree in astronomy from the University of Bologna, Italy, in 1997 and 2002, respectively. From 2002 to 2005, she was a Postdoctoral Fellow at the University of Bologna. Since 2008, she has been a Postdoctoral Fellow at the INAF—Osservatorio Astronomico di Cagliari, where she has been a Researcher, since 2008. Her research interests include extragalactic radio astronomy, with major contributions in galaxy clusters and large-scale magnetic fields in the universe. She is currently a Coordinator of the Radio Astronomical Division of the INAF Scientific Directorate and the Scientific Coordinator of the project ''The Enhancement of the Sardinia Radio Telescope (SRT) for the study of the Universe at High Radio Frequencies.''

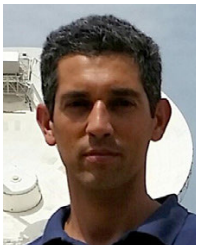

M. MURGIA received the Ph.D. degree in astronomy from the University of Bologna, in 2001. He is currently a Senior Researcher at the National Institute of Astrophysics, INAF—Cagliari Astronomical Observatory. His most important contributions concern the studies of the evolution of extragalactic radio sources, the radio emission from galaxies with intense star formation, and the estimation of the magnetic field on a large scale in galaxy clusters. The results of these researches, also achieved thanks to the development of dedicated software, are summarized in about 140 publications in refereed international journals. In parallel with his research commitment, he held teaching positions in the degree courses in astronomy and physics, respectively, at the Universities of Bologna and Cagliari, and supervised several graduate students, Ph.D., and postdoctorates. He has been a Co-Project Scientist of the scientific development of the Sardinia Radio Telescope and a PI of the Sardinia Array Demonstrator Project, a low-frequency array composed of 128 Vivaldi antennas deployed at the SRT site. He is involved in the high-frequency upgrade of the SRT as the Scientific Manager of MISTRAL, a millimeter camera composed of 408 kinetic inductance detectors.

E. CARRETTI is currently a Senior Research Scientist at INAF Istituto di Radioastronomia, Bologna. Formerly, he was at INAF IASF, Bologna; CSIRO Astronomy and Space Science, Parkes and Sydney; and INAF Osservatorio Astronomico di Cagliari. He has covered management roles for projects and facilities, such as a Project Manager of the space project SPOrt, a System Scientist of the Parkes Radio Telescope, and an Officer in Charge of the Sardinia Radio Telescope. He is currently a part of many international collaborations, among which ASKAP POSSUM, LOFAR MKSP, GMIMS, and ASKAP EMU. His research interests include architectures for radio polarization receivers, the large scale structure of the Milky Way, and magnetism of the large scale structure of the universe.

D. FIERRO graduated in mechanical engineering from the University Federico II of Naples. He received the Ph.D. degree in industrial/management engineering from the University Federico II of Naples. He has about 25 years' experience in systems engineering and project management disciplines with his first role as a VST Telescope Deputy Project Manager, in 1997. He spent about two years at ESO Observatory in the Atacama Desert, Chile, where he was also responsible for the integrating and testing activities of the VST telescope. As the Head of INAF's Engineering Office, he has chief technical/managerial responsibilities in several international projects as Square Kilometer Array (SKA) of which he has been the Program Manager of the whole Italian technical participation. He is currently fully involved as a Program Manager in the overall refurbishment/upgrade projects of the SRT Sardinia Radio Telescope and he coordinates the INAF's involvement in the European Space Surveillance and Tracking (SST) Program in close synergy with the Italian Space Agency and the Italian Ministry of Defense. He collaborates with the Project Management Institute and with various universities in disseminating systems engineering and project management discipline. He is/has been a member of the Defense, Security and Space Committee of PMI, Space Situational Awareness working groups of research and defense ministries, the TLI Technical Leadership Institute of INCOSE, and boards of several international projects, such as SKA-LFAA. He is an INCOSE CSEP—Certified Systems Engineering Professional. He is certified by the Italian Institute of Project Management—ISIPM.

A. PELLIZZONI was born in Milan, Italy, in 1971. He graduated in physics (Hons.), in 1997.

His formation and career involved activities related to astrophysical instrumentation development, operation and management, and scientific research, collaborating with major institutions in Italy, such as the National Research Council of Italy (CNR), the Italian Space Agency (ASI), and the National Institute for Astrophysics (INAF), where he has been serving as a Permanent Staff Researcher, since 2008. He worked as a Lecturer at the University of Cagliari (on observational astrophysics and techniques). In the period of 2008–2011, he was a part of the Scientific Council of INAF, as a member elected by the scientific community. He has contributed to instrument simulations and calibrations, development of scientific data analysis tools for ground-based facilities (in particular the Sardinia Radio Telescope, SRT), and space missions (for example the gamma-ray satellite AGILE). His scientific results are mostly related to multi-wavelength studies (from radio to gamma-rays) of compact Galactic sources, such as Neutron Stars and Black Holes and their environment (Pulsar Wind Nebulae, Supernova Remnants, and Galactic extended emission). He is the author of over 120 refereed publications on the above subjects. Since 2017, he has been focusing on a new challenging technological and scientific project: the development of radio solar imaging techniques and instrumentation for the monitoring of the Sun using the INAF radio telescopes (https://sites.google.com/inaf.it/sundish). He is a member of the INAF board dedicated to solar physics science and related space weather applications.